

Sedimentary record of historic seismicity in a small, southern Oregon lake

Ann E. Morey (Ross) (✉ ann@cascadiapaleo.org)

Cascadia Paleo Investigations <https://orcid.org/0000-0002-8702-2581>

Mark D. Shapley

Continental Scientific Drilling Facility, University of Minnesota School of Earth and Environmental Sciences and The National Science Foundation, 116 Church St SE, Minneapolis, MN 55455

Daniel G. Gavin

University of Oregon, Eugene, OR

Alan R. Nelson

Geologic Hazards Science Center, U.S. Geological Survey, Golden, Colorado 80401 (retired)

Chris Goldfinger

Oregon State University, Corvallis, OR

Research Article

Keywords: lacustrine paleoseismology, Cascadia Subduction Zone, paleohydrology

Posted Date: May 9th, 2022

DOI: <https://doi.org/10.21203/rs.3.rs-1631354/v1>

License: © ⓘ This work is licensed under a Creative Commons Attribution 4.0 International License. [Read Full License](#)

Abstract

We compare disturbances from the historic portion of the sedimentary record from Lower Squaw Lake, Oregon, to the historic record of events from the region to (1) determine if the lake records Cascadia megathrust earthquakes, and (2) if sediment deposits can be differentiated by disturbance type. We use the sedimentological characteristics and geochemically inferred provenance of the deposits (labeled A-J) from the historic portion (post 1650 CE) of the record to discriminate between types of deposits.

We show that earthquake-triggered deposits are complex and flood deposits are simpler but vary depending on flood characteristics. Disturbance deposit J dates close to 1700 CE (1680–1780 CE) through multiple approaches. This deposit suspected to result from the magnitude (M) 8.8–9.2 1700 CE Cascadia megathrust earthquake is composed of unusually well-sorted, normally graded, medium-grained silt derived from distal rocks in the upper watershed. The silt grades upward, increasing in organic content forming a long, organic-rich tail. Load structures of silt into the organic-rich sediment below suggest rapid deposition. In contrast, a deposit attributed to the ~M7.0 1873 CE intraplate earthquake is a normally graded, medium-grained, watershed-sourced silt overlain by a thinner organic tail and preceded by a deposit interpreted as a local wall failure. These results suggest that inland lakes can be sensitive recorders of earthquakes, and that it is possible to discriminate between plate margin and other types of earthquakes, and floods.

Introduction

Approach

Lake sediments can provide high resolution, continuous records of earthquake-triggered disturbances (Goldfinger et al., 2017; Howarth et al., 2014; Moernaut et al. 2007; Monecke et al., 2004; Praet et al., 2017; Strasser et al., 2013). Lakes are also good recorders of other types of disturbances, such as floods (Gilli et al., 2013; Wilhelm et al., 2013, 2018), postfire erosion (Colombaroli et al., 2018), flood-induced erosion (Howarth et al., 2012) and wildfires (Bradbury, 1996; Long et al., 1998; Colombaroli et al., 2010; Hennebelle et al., 2020). Lake sediments in Cascadia are increasingly exploited for their paleoseismic potential (Leithold et al., 2018, 2019; Goldfinger et al., 2017; Morey et al., 2013); however, most other studies that have examined the differences between earthquake-triggered deposits and those from other types of disturbances are from large lakes (>100 km²). Understanding the influence of Cascadia earthquakes on lakes is crucial because researchers have long suspected an influence from megathrust earthquakes in Cascadia lakes in the Oregon Coast Range (Long et al., 1998), Lake Washington (Karlin & Abella, 1992, 1996; Karlin et al., 2004), the Olympic Peninsula (Leithold et al., 2018), Seattle area (Goldfinger et al., 2017), and in the Klamath Mountains and Coast Range of Oregon, (Morey et al., 2013). Understanding the impact of megathrust earthquakes in Cascadia lakes has the potential to both provide insight into Cascadia earthquake behavior and improve the interpretation of proxy data.

Differentiating between flood and earthquake-triggered deposits can be challenging. Some research suggests that flood-triggered turbidites are more evenly distributed throughout the lake and earthquakes are thickest in the lake's depocenter (Vandekerkhove et al., 2020, and references therein). Other studies show that flood deposits exhibit reverse, then normal, grading in contrast to the normal grading of turbidites (Mulder et al., 2003; St-Onge et al., 2004; Beck, 2009; Wirth et al., 2011) or contain larger clastic particles compared to background sediment (Toonen et al., 2015; Schillereff et al., 2014; Campbell, 1998). Many factors contribute to the characteristics of the resulting deposits (particle size, clastic supply, slope angle, basin shape and slope stability, etc.), therefore each lake must be evaluated independently.

To determine if small (<10 km²) lakes record evidence of Cascadia earthquakes and ascertain how the resulting deposits differ from other types of disturbance deposits (such as flood deposits), we investigated the sedimentary record from Lower Squaw Lake, Oregon, located ~180 km inland of the Cascadia subduction zone trench. Our approach was to compare the historic portion of the sedimentary record to the record of extreme events known to influence the region. The lake is an ideal study site because it has experienced extreme events, including earthquakes and floods, and the bedrock that immediately surrounds the lake is locally distinctive from the bedrock of the steep watershed that contributes sediment to the north end of the lake. This

heterogeneity of watershed bedrock is important because it provides an opportunity to determine the sediment provenance and possible mechanisms controlling deposition. It is also located adjacent to Upper Squaw Lake, which has an existing record of watershed disturbances, some of which are already suspected to be the result of Cascadia earthquakes (Morey et al., 2013; Colombaroli et al., 2018).

Background

Setting

Upper and Lower Squaw Lake (42°01'55" N, 123°00'56" W) are located in the Siskiyou region of the Klamath Mountains, ~180 km inland of the trench (the surface expression of the Cascadia Fault; Figure 1, top left), at an elevation of ~920 m. The lakes formed when a landslide dammed Squaw and Slickear Creeks near their confluence, creating two basins draining watersheds of different sizes and bedrock types. The lakes are located near the southern extent of the Cascadia subduction zone, just inland of the boundary between the obliquely subducting (~27-45 mm/yr) Juan de Fuca Plate and the deforming Gorda Plate (Figure 1), ~200 km north of the northward migrating Mendocino Triple Junction. The lakes are ~35 km above the inferred location of the transition from seismic to aseismic slip on the Juan de Fuca Plate (Figure 1, left; McCrory et al., 2014; Yeats, 2004) near the zone of maximum episodic tremor density (see Figure 1 in Wells et al., 2017).

The most likely sources of regional seismicity with the potential to disturb Lower Squaw Lake sediments are earthquakes within the subducting plate, megathrust earthquakes on the plate interface, and earthquakes on crustal faults in the overriding North American plate. The USGS Quaternary Fault and Fold database for the United States (with additional information from the California Geological Survey) for the United States (accessed May 2019, <https://earthquake.usgs.gov/hazards/qfaults/>) identifies few active regional faults, however the simplified Cascadia forearc fault model of Wells et al. (2017) identifies a fault along the Klamath River, just south of Squaw Lakes (Figure 1, right).

The largest historic earthquake in Oregon was a ~M7 earthquake that occurred on November 23, 1873 (Wong, 2005). This earthquake was strong enough to topple chimneys in Jacksonville, OR, 15–20 km east of Squaw Lakes (Ellsworth, 1990) and has been interpreted as an intraplate earthquake primarily because of the lack of reported aftershocks (Wong, 2005). Numerous investigations of felt reports published in regional newspapers suggest the intensity center was located ~10 km inland from the coast, from just south of Cape Blanco, OR, to Crescent City, CA (Bakun, 2000; Topozada et al., 1981). Brocher (2019) suggested the intensity center was located roughly halfway between Grants Pass, OR, and the coast, ~75 km west of the study site.

Both Upper and Lower Squaw Lakes are surrounded by Condrey Mountain Schist ("lake bedrock," dark gray unit in Figure 2), a heavily foliated quartz-muscovite schist (Hotz, 1979), that has been described as failure-prone (Coleman et al., 1983). The northern portion of Lower Squaw Lake is fed primarily by Slickear Creek, which is almost entirely located in a unit mapped as metavolcanics sediment and flows (andesite) and quartz-diorite ("watershed bedrock," orange unit shown in Figure 2). The watershed rocks have a different composition and are more resistant to erosion than the schist that surrounds the lakes and most of the Squaw Creek watershed.

Climate

The Klamath Mountains ecoregion experiences a Mediterranean climate characterized by hot dry summers and wet winters (Sleeter & Calzia, 2012). The wet winters are the result of equatorward shifts in midlatitude storm tracks during the winter months (Swain et al., 2018). The latitude at which this shift occurs is variable through time and can result in extreme shifts between flooding and drought (Horton, et al. 2015). Atmospheric rivers are narrow pathways of tropical moisture that are regionally important because they provide a large amount of rainfall and stored water in the form of high-elevation snowpack to the region (Goldenson et al., 2018). Sustained atmospheric river events can produce extreme flooding (Safeeq et al., 2015), such as occurred during the 40-day event that occurred in 1861–1862 (Engstrom, 1996).

Sediment transport

For the post-logging era (1930–present) the dominant influence on sediment accumulation rates identified from the sedimentary record from Upper Squaw Lake is rainfall (Colombaroli & Gavin, 2010; Colombaroli et al., 2018). Prior to that, the largest accumulation rates are related to postfire erosion and possibly earthquakes, as part of complex feedbacks (Colombaroli & Gavin, 2010; Colombaroli et al., 2018). Slope failures and slumps around Lower Squaw Lake are common on the steep hillslopes and were observed as changes in the landscape and vegetation, suggesting possible instability during shaking. Rainfall, the dominant influence on slope wash from hillslopes to streams in upland regions (Lamoureux, 2002; Zolitschka, 1998), occurs primarily during the wet season from November to April (Sleeter & Calzia, 2012). Stream bank outcrops suggest occasional extreme, erosive flow. Snowmelt floods, which occur when rain-on-snow events melt snow in the upper reaches of the watershed, may also introduce pulses of sediment into the lake. Flash floods have been observed to transport and deposit sand to boulder-sized particles near Slickear Creek to the north near the lake margin where vegetation is dense (Bert Harr, personal communication, September 2015; landowner).

Lake and watershed characteristics

Lower Squaw Lake is a long, narrow (area = 22.6 ha), deep (~40 m) lake at 915 m elevation. The Slickear Creek watershed to the north is smaller (7.7 km²) than the Squaw Creek watershed to the east (40.2 km²). The level of Lower Squaw Lake was raised above its natural level by ~5 m in 1877 when a dam was built to increase water pressure for hydraulic gold mining (*Jacksonville Times*, September 25, 1878). The ~0.5 km long Slickear Creek delta is composed of coarse sand, cobbles, and a few boulders near the shore of the lake where vegetation is dense. The delta has been built rapidly by floods that have occurred every ~10–20 years, occasionally depositing a thick layer of coarse sediment over the entire delta (Bert Harr, personal communication, September 2015; see Table 1). Most of the water flows into the lake from the north as subsurface flow; however overland flow occasionally occurs along the small (a few meters wide) but incised stream channel on one side of the delta.

Upper Squaw Lake is a small (7.3 ha), shallow (14.2 m) lake at ~930 m elevation with a capacity of ~564,000 m³. Upper Squaw Lake drains a large watershed (40 km²) of steep terrain (~1,020 m relief), and the creek flows throughout the year through Squaw Creek into the southern portion of Lower Squaw Lake near the dam. Although the terrain is steep throughout much of the watershed, the proximal ~2.0 km near Lower Squaw Lake becomes gently sloping, and the creek meanders and branches as it nears the lake, then enters the lake over a delta front composed of angular, well-sorted, medium to coarse sand. Groundwater likely flows through the delta, as water-tolerant trees and shrubs are present. Two sediment cores with overlapping sections were taken from near the center (water depth of 14.1 m) of the lake and were used to create a composite depth profile of a high-resolution 10 m sediment core containing a record of watershed-sourced deposits over the past ~2,000 years (Colombaroli & Gavin, 2010; Colombaroli et al., 2018).

The Atlas of Oregon Lakes (Johnson, 1985) describes Lower Squaw Lake as an unusually deep lake for its size, with a high concentrations of ions, especially of calcium and magnesium. Alkalinity and conductivity are also high, with pH value of 8+. It has been classified as a mesotrophic to oligotrophic lake based on a secchi disk depth of 6.2 m. The lake shows evidence of oxygen depletion at depth. A phytoplankton sample taken on 7/13/82 identified the dominant species as *Ceratium hirundinella*. Also present was *Dinobryon sertularia*, *Melosira granulata* and *Asterionella fomsa*. Water column measurements of temperature, oxygen and specific conductance were acquired in 2014 (this study) which are presented in Figure 3 (right) along with the water column data collected by Larson et al., 1975.

Upper Squaw Lake continuously overflows into Lower Squaw Lake through Squaw Creek. Water accumulates in Lower Squaw Lake from upper and lower lake catchments (Figure 3, left). Local people and Forest Service employees observed flood waters in 1997 filling Lower Squaw Lake to capacity, forcing water, sediment, and downed trees to the south, blocking the outflow and raising the lake level above the dam (Peter Jones, personal communication; January 2020). Accounts of this event describe Lower Squaw Lake was described during this event as a wide, fast flowing stream that undercut the lake shore resulting in soils and colluvium to slump into the lake.

Methods

Sediment cores

We collected sediment cores from Lower Squaw Lake during the summers of 2013, 2014, and 2015. We used a modified Livingstone corer (Wright, 1967) deployed from a custom platform fitted with a stainless-steel pipe attached to two inflatable rafts (2013) or canoes (2014), to collect Cores 1, 2, and 4,5 (overlapping drives at a single location). We used a Kullenberg piston corer (Kelts et al., 1986) to collect cores in 2015 and collected surface samples from the same locations with a gravity corer, both deployed from an aluminum platform supported by two 7-m skiffs (LacCore; 2015). We acquired single-beam bathymetric data in May 2015 by canoe fitted with a Garmin GPS-enabled “fish finder” and receiver.

Sediment properties

We described the sedimentology and deposit characteristics of core sediment using the following data types: Munsell color, sediment texture, composition (microscopic analysis of smear slides), and grading and contact characteristics (sharp, gradational, discontinuous, etc.). We acquired particle-size data at 0.5 cm intervals through disturbance deposits, and less frequently between them. We measured volume magnetic susceptibility (k) using a Bartington MS2E point sensor at 0.5 cm resolution. We acquired combustion data at 0.5–1.0 cm intervals through disturbance deposits and less frequently elsewhere, resulting in data for percentage of inorganic content (clastic particles other than CaCO_3), percentage of organic matter, and percentage of CaCO_3 (calculated from dry weights). We acquired CT imagery and data using the Toshiba Aquillon 64 slice CT unit at the Oregon State University Veterinarian Hospital (at 0.5 mm resolution). Mineralogy was spot-checked as needed using the LacCore desktop scanning electron microscope (Hitachi TM-1000).

Identification of Disturbance Deposits and Lithostratigraphic Correlation

We identified disturbance deposits in cores as abrupt increases in petrophysical property data (magnetic susceptibility and CT density imagery and data) in contrast to the typical organic-rich background sediment, then used lithostratigraphic methods to correlate units between cores. Petrophysical properties typically reflect the vertical grain size distribution of the particles of the deposits in marine cores (Kneller and McCaffrey, 2003; Goldfinger et al., 2012; Patton et al., 2015) and lake cores (Karlin and Seitz, 2007), however they have also been shown to also reflect the inorganic content in lake cores dominated by organic sedimentation (Morey et al., 2013).

Lithostratigraphic correlation takes advantage of the characteristics of both the sequence pattern of disturbances as well as the characteristics of the petrophysical properties through the disturbance deposits themselves. The petrophysical properties of the disturbance deposits can be considered fingerprints of the time history of deposition of the disturbance deposit (Goldfinger et al., 2008, 2013; Patton et al., 2015), and individual disturbances from independent records have been shown to correlate over long distances even though they are from different depositional settings (Goldfinger et al., 2012; Morey et al., 2013). Density is the highest resolution petrophysical property data type, has been shown to be the most sensitive property to changes in fine-grained inorganic disturbances (Inouchi et al., 1996), and does not as much of an edge effect that magnetic susceptibility data has (because of the higher resolution), therefore the high-resolution CT density was heavily relied upon for correlation.

Sediment provenance data

We used x-ray powder diffraction (XRD) spectra to determine the mineralogy of the two endmember bedrock types. XRD allows qualitative and semiquantitative analysis of the mineralogy of sediments and rocks by measuring the diffraction properties of their mineral components. We interpreted the results using the automated pattern-matching routine in Jade Software (<http://ksanalytical.com/jade-9/>), which compares the relative peak heights and areas from unknowns to those from samples of known mineralogy contained in the software database.

We acquired x-ray fluorescence data (XRF) with an ITrax core scanner (Oregon State University) from downcore sediment at 0.4 mm intervals and from discrete samples of lake-margin beach sand and Slickear Creek streambed sand (source locations are shown as blue triangles in Figure 3, left). The XRF downcore data were used to determine the upper and lower boundaries of each deposit in addition to identifying sediment provenance.

Development of event-free stratigraphy and age-depth model

Event-free stratigraphy. Rapidly deposited sediment was removed from the stratigraphic sequence to avoid misinterpreting it as being deposited through time. This event-free stratigraphy was created by identifying the disturbance deposit boundaries using XRF and estimating missing sediment at erosional contacts. XRD data from endmember rock samples were used to initially determine the best choice of elemental variables to use as XRF provenance indicators. XRF variability through the disturbance deposits was then used to determine where deposit boundaries exist. Sharp increases in sediment density (higher HUs; lighter values), compared to lower density background sediment (lower HUs; darker values), indicate rapid deposition or reworking as described in Morey et al. (2013).

Radiocarbon samples and data. We sampled Lower Squaw Lake sediment cores for radiocarbon dating after splitting cores longitudinally. We removed macroscopic samples of fragile plant material (such as fir needles and buds) from the targeted horizons of undisturbed sediment, cleaned and dried them, then had them analyzed by AMS (accelerator mass spectrometer) for radiocarbon. We selected the target horizons for sampling based on a suspected temporal tie point between the Lower Squaw Lake record and the dated sequence from Upper Squaw Lake. We did not acquire ^{210}Pb and ^{137}Cs data to calculate sedimentation rates for the most recent section of the cores because the upper portions of the sediment cores contained two thick clastic units (lake-wide and of varying thickness) with evidence of erosion, which violates the dating method assumption of continuous sedimentation. We used the strong similarity in sequences between the upper and lower lakes to infer that the younger of these clastic disturbance deposits was deposited close to 1964–1965 (as shown in the Supplementary Data).

Age-depth model. An age-depth model was developed using a Bayesian approach using OxCal (v 3.4.2; Bronk Ramsey, 2017). Age-depth modeling is challenging for the most recent 300 years because of the variability in the radiocarbon production curve (Figure 4).

Results

The historic record of extreme events

Historic events with the potential to influence Lower Squaw Lake sedimentation are compiled from personal accounts (from landowners and U.S. Forest Service Rangers), published hydrologic data, regional historic newspapers, and Forest Service documents (Table 1). We did not include large land-use events (logging efforts and road building) or wildfire in Table 1 because these events require water to transport the resulting increase in available sediment into the lake, however extreme runoff from these types of events can cause debris flows (Wall et al., 2020). Settling began in the region when gold was found between 1850-1852 CE (Lalande, 1995).

Sediment core locations and recovery

This study investigated historic records from the northern cores (Figure 5; orange circles) near the Slickear Creek delta, which is saturated near the surface. Sediment core locations, lengths and water depths are shown in Table 2. Several of the upper sections of the first Kullenberg cores were distorted during coring and stuck in the casing. Small adjustments to composite sediment depths accounted for core section breaks and minor distortion.

Sediment facies

Background facies. Background sediment is a very dark brown to black (Munsell color: 2.5YR 2.5/1) organic-rich sediment containing planktonic diatoms (~30%), particulate organic matter, and angular, poorly sorted medium to coarse silt (50–60%).

Split sections change color quickly (over a period of hours to days) from very dark brown (or black if the core was taken in deep water) to a lighter brown, or slightly orange color and become concreted if exposed to air. Background sediment is stiffer and slightly lighter in color deeper in the cores compared to the sediment in the upper portion of the cores. This change in upper sediment character was assumed to be due to historic land-use changes that began between 1850 and 1900 and the installation of the dam in 1877. A shift in sediment density occurs below the two thick upper deposits in all cores. This horizon, indicated in the table as "inflection," refers to the change in sediment density that is suspected to reflect changes in sedimentation from around the time settlers cleared land (mid 1800's) and built the first dam (1877 CE). Loss on ignition and physical property changes associated with this shift are shown (data are from core SQB2; Table 3).

Disturbance facies. Ten disturbance deposits from the sediment cores were identified as abrupt increases in sediment density compared background levels (based on the downcore CT data). The disturbances identified in core SQB5 using this method are labeled A–J in Figure 6. Disturbance event facies are inorganic layers (> 80% clastics of total by weight) of two primary types: a lighter gray (Munsell color: 2.5Y 4/1) medium-grained silt without visible mica flakes, and a darker gray (Munsell color: Gley2 4/5PB) coarse micaceous silt. We observed two thick (5–25 cm, depending on core location and water depth), visually similar, massive to normally graded silt units in the upper ~100 cm of each core.

A third type of disturbance facies is one that is slightly denser than background sediment with little change in magnetic susceptibility, and although visible by eye, not identifiable as different by Munsell color. This facies type is more common in the cores but is generally thinner compared to the other types of disturbance facies.

Characteristics of disturbance event deposits A-J

Deposits A and B. Deposits A and B are thick units (5–20 cm, depending on the location of the core in the lake; Figure 7) with sharp basal contacts. These disturbances are found throughout the lake. They vary with distance from Squaw Creek in the south: deposits are thicker and more complex to the south and show evidence of erosion in all cores except those recovered from near the lake's depocenter (cores SQB9 and SQB10). Interevent sediment sections are also thicker and more complex in the south. Basal sediment contains rootlets and other particulate and degraded organic matter (Figure 8). Grading proceeds from poorly sorted coarse silt and fine sand upward to well-sorted fine-medium silt, followed by a thin, poorly sorted multimodal fine silt and thin (< 1 cm) silty-clay tail. The deposits are gray (2.5Y 3/2), however, the lower half of deposits A and B are browner compared to the upper half of the deposit. Smear-slide inspection suggests this brown color is from degraded organic matter entrained in the sediment. Magnetic susceptibility is highest near the top of the sequence, just below the silty-clay cap. Although deposits A and B have similar characteristics, the base of deposit A has a thin layer of lighter-colored coarse silt-fine sand without visible mica, which was not observed at the base of deposit B. The presence of rootlets and broken diatoms in the lower portion of the deposit and sharp contact indicate erosion and reworking of lake-margin sediment.

Deposit C. Deposit C is a fine-grained (medium silt), light-colored (5Y 2.5/2) unit that is wavy and discontinuous. It is thin (<1 cm) and becomes thinner with distance from Squaw Creek but is thicker (~3 cm) and slightly brown (but still 5Y 2.5/2) in color in core SQB15. It is present in all cores except for core SQB5.

Deposit D. Deposit D is a sequence of three thin (<0.5 cm) wavy medium silt layers in background sediment that is slightly stiffer than the surrounding sediment. The basal layer is distinctive because it is orange (5Y 4/1).

Deposit E. Deposit E is a thin (~1 cm) dark gray (GLEY2 4/5PB) medium-grained, poorly sorted silt deposit containing visibly large mica flakes. This deposit is present only in core SQB5. The deposit has a sharp base and is normally graded. We observed rootlets and other organic matter, particulate and degraded, near the deposit base.

Deposit F. Deposit F is a slightly lighter gray (compared to background, 5Y 2.5/2), normally graded, medium silt unit with a sharp basal contact. Both magnetic susceptibility and CT density are higher than background sediment, suggesting a high concentration of inorganic particles, supported by the loss on ignition data of a 5% increase in inorganic content compared to background (data from SQB2A). Loading of this silt layer into the organic sediment below suggests rapid deposition of denser sediment (most obvious in the CT scan of SQB2A at about 40 cm depth in Figure 9, but also shown at the top of Figure 10).

Deposit G. Deposit G is visually indistinct with a rounded CT density profile (see CT density trace in Figure 10a). There is little change in magnetic susceptibility through the deposit. It is ~3 cm thick (based on CT density) and found in all the northern cores. Smear-slide data do not show any visible differences in composition through the deposit, however a 2-3 percent increase was observed in the inorganic content. The base and top are indistinct; peak density occurs at the midpoint of the deposit.

Deposit H. Deposit H (Figure 10) is slightly lighter gray (2.5Y 4/1 at the very base) and appears slightly stiffer than background sediment. It is a thick unit (basal silt is ~1 cm and density suggests the deposit may be up to ~4 cm in Core SQB2) with normal grading and a sharp basal contact. Grading proceeds from poorly sorted medium silt upward to a more well-sorted medium silt, and loss on ignition data indicate an upward increase in the ratio of organics to inorganics with grading. This deposit tail appears mottled in the CT density imagery. Deciduous leaves were observed at the basal contact in some of the cores.

Deposit I. Deposit I (Figure 10b) is a dark gray (GLE2 4/5PB) coarse silt dominated by large, visible mica flakes (~90% inorganic). The deposit has a sharp basal contact and is initially reverse, then normally graded. The reverse-graded portion of the deposit has a higher percentage of organics (including rootlets) compared to the normally graded portion of the deposit. The base of the deposit is very sharp with evidence of erosion (truncated beds). A comparison to other cores indicates missing sediment below it, more so in SQB1, SQB2 and SQB14 compared to SQB5. Deposit characteristics (mica-rich graded deposit) are similar to deposit E; however, unlike deposit E, deposit I is found throughout the lake.

Deposit J. Deposit J (Figure 11) is a lighter gray (2.5Y 4/1) silt unit. It is thick (~7-15 cm), dense (~1,000 HU at the base), weakly graded, medium to fine-grained silt unit with a long tail. The silt is fine-grained and well-sorted (~90% inorganics) at the base lacking other components such as reworked diatoms and organic matter. The visible layer of silt is 3–4 cm thick and becomes less well sorted (but not finer grained) upward. Percentage of organic matter increases upward with fining. There is evidence of loading of the silt into the less-dense sediment below (Figure 9, right), suggesting rapid deposition, of the silt into the less-dense sediment below. Loading can be seen in more detail further downcore (Figure 10c).

There are ten total disturbance deposits of the following types:

Type 1 deposits (deposits A and B, possibly C) are thick graded turbidites of mixed sediment composition. The disturbance deposits are composed primarily of coarse silt and have erosive bases containing organic matter at the base, fining upward with a thin clay cap and no perceptible grading of organic content in a tail. The disturbances do not show evidence of loading into the sediment below.

Type 2 deposits (deposits E and I) are schist turbidites with erosive bases and no evidence of loading into the sediment below. These schist turbidites have an organic-rich tail.

Type 3 deposits (deposits H and J) are composed of watershed sourced sediment containing a thick well-sorted medium silt layer with evidence of loading into the organic sediment below. There is no evidence of erosion at the base and only trace amounts of organics and diatoms. The silt grades upward with respect to organic content for several centimeters. The post-tail sediment contains a different community of diatom species and other organisms and is of lower CT density compared to background sediment.

Type 4 deposits (deposit G and unnamed deposit below deposit J) are ungraded deposits with mixed composition and rounded density profiles. Although the density of the unit is higher, the composition of sediment is similar to background, suggesting an increase in clastic content of mixed sources.

Deposits D and F are difficult to characterize because they are thin layers that are challenging to sample for grain size and composition. The base of deposit D is orange in color, composed of watershed sourced silt (basal silt layer), and has three silt layers within slightly stiffer background sediment. Deposit F is slightly lighter in color compared to background and shows evidence of loading onto the organic sediment below. Neither deposit shows evidence of erosion at the base.

Radiocarbon results

Radiocarbon determinations are shown in Table 4. Samples 6, 7 and 8 are included here even though they are more than 1000 ¹⁴C yrs BP because they provide a key temporal tie point between the cores. Sample 0 was not included in the age model because it is much older than the others in the sequence (suggesting it does not represent the time of deposition). Samples 1-4 were used to create the age-depth model for the historic portion of the core, and samples 5-7 are included here to show the temporal relationship between cores at the lower end of the section used in the age-depth model. Note the close similarity in ages between samples 6 and 7.

Composite core section and correlation points among cores

We used the radiocarbon ages from detrital plant fragments (Table 4), core imagery and descriptions and physical property data to (a) create the composite core, SQB1/2/ss, for the historic portion of the Lower Squaw Lake record, and (b) identify stratigraphic tie points for the northern cores (Figure 12). CT density was heavily relied upon for correlations because of its very high resolution (sub-mm scale) as described in the Supplementary Data (Figure 12a inset). Little sediment is missing between each 1 m section in core SQB2, based on a comparison to SQB1, therefore only section, SQB1A, was needed to complete the splice. We used the surface sample (ss) to reconstruct the two upper disturbances because they are missing from the top of SQB2 and SQB1. Note that only the northern cores were used for the splice because core length differences from north to south suggested large changes in sedimentation rate.

The radiocarbon data were used to tentatively link cores for the splice. The numbered stars in Figure 12a identify the locations of radiocarbon samples 1–3 (Table 4). We used additional radiocarbon data (samples 4–8) to create the tie points and splices but did not include them in the age model for the historic record because they predate it. The radiocarbon age for Sample 0 (gray text) is too old (reversed) for the sequence and we did not use it. We identified the historic portion of the record as just younger than Sample 3 because this radiocarbon age likely represents a horizon that is older than the 1700 CE earthquake. We used this horizon to define the lower boundary of the historic section of the record. A splice table (Table 5) shows the depth equivalencies of sections used to create the composite core. Note that the length of SQB-ss was adjusted to match the stratigraphy of SQB2-A (see Figure 12a). The age model was created using the upper 2.5 m of the composite section. Sections showing significant erosion are the surface samples; these cores are shown in false color (far left) to highlight the stratigraphy and to improve the identification of erosional contacts and missing sediment.

Tie points lake-wide were created using the distinctive sequence of disturbances in the record using core-log correlation and radiocarbon data where these data were available (Figure 12b). The distinctive sequence includes two, thick upper disturbances, followed by one disturbance with two at the very end of the sequenced used for the upper portions of the cores. The relationship between the Lower Squaw Lake and Upper Squaw Lake sequences is shown (Figure 12b, left).

Sediment Provenance Data

X-ray Diffraction Spectra. We identified provenance endmembers by XRD analysis of watershed and lake bedrock samples (Table 6; data available in the supplementary data). The bedrock that surrounds the lake is composed of a quartz muscovite schist with chlorite minerals, similar to what has been mapped, whereas the Slickear Creek bedrock is composed of Ca- and Fe- amphibolites, chlorite minerals and albite. We also analyzed samples of silt from the upper portion of core SQB2, and a sample of gravel from the base of the core. Results confirmed a schist source for the dark gray silt layers containing visibly large mica flakes, and a watershed source for the lighter gray silt and basal gravel samples. Inspection by Energy-dispersive x-ray spectroscopy (Bruker Quantax 50 EDS; CSD Facility) showed that some mica flakes from the Condrey Mountain Schist surrounding the lake contain a large amount of carbon (as much as 77%) and scanning-electron-microscopic analysis shows the presence of pyrite. This finding suggests that some of the schist is likely graphitic, which (along with pyrite and reduced manganese) may contribute to the black color of sediment.

Sediment Provenance Data

X-ray Fluorescence. The downcore X-ray fluorescence (XRF; core SQB5) data and results from the analysis of individual sand samples (from locations identified as blue triangles in Figure 3) are shown in Figure 14. Figure 14 (left) shows that, as expected, the raw counts for elemental variables covary downcore with CT density and magnetic susceptibility, especially iron, silicon, and potassium. Some deviations from this relationship emerge, however. For example, whereas most elements covary with sediment density, deposit E and deposit I do not have coincident increases in calcium and manganese with CT density. Virtually no overlap exists between the samples of sand surrounding the lake and the Slickear Creek bed sand, regardless of whether it was normalized by titanium, strontium, or left as raw counts. This lack of overlap between Ca versus K in the scatterplots of the XRF data from lake margin beach sand and watershed streambed sand (Figure 14, right) is consistent whether data are represented as peak areas (raw counts, top) or normalized by titanium (middle) or strontium (bottom).

Each of the event deposits identified are shown as separate scatterplots in Figure 15. These scatterplot patterns are different in terms of direction in which the deposit evolves (clockwise or counterclockwise), in terms of direction with respect to the axes, and finally, the changes in one variable with respect to the other. Most of the disturbances (deposits B, D, E, F and I) show counterclockwise rotation whereas deposits J and H rotate clockwise. Those with clockwise rotation are also those enriched to some degree in Ca compared to the counterclockwise deposits which are enriched relatively in K. Deposit J is the only deposit that shows complex variability because it increases parallel to background, then crosses, then returns.

Age-depth Model

We created the age-depth model using the radiocarbon ages (samples 1-4) in Table 4, the event-free stratigraphy (shown in Figure 12a) for SQBss/1/2, and erosion estimates using a P_sequence in OxCal (v 3.4.2; Bronk Ramsey, 2017) as described in the methods section. We use a k value of 1 (typical for cm scale sedimentation rate variability to allow changes every 1 cm) and then define a prior for $\log_{10}(k/k_0)$ that allows variation by 2 orders of magnitude. The goal of this is to allow some flexibility in the age model to account for a variable sedimentation rate. The upper end of the record is constrained based on the sediment inflection representing approximately the time of land use changes in the mid 1800's (Lalande, 1995; including the raising of the lake level in 1877; see inflection in sediment density in Figure 6) and using the assumption that deposit B was deposited in 1964. The 1964 horizon was determined based on a comparison of the upper and lower lake records (as detailed in the Supplementary Data). The resulting modeled and unmodeled age ranges, and agreements between them, are shown in Table 7a. For comparison, the same information is shown for the same model, but instead of sample 2 a calendar date of 1700 CE is used (Table 5b). The resulting model and estimated age ranges for event deposits A-J are plotted as shown in Figure 16 and listed in Table 8.

Discussion

This study seeks to determine if sediments from Lower Squaw Lake, Oregon, contain evidence of Cascadia earthquakes. To address this, we evaluate the timing and characteristics of the disturbances in the sedimentary record, starting with deposit J, which is suspected to have been deposited in response to the 1700 CE Cascadia earthquake. Each deposit includes a reference to the age-depth model (Fig. 16) and resulting modeled calendar ages for each of the deposits in the sequence. First, however, we summarize likely types of disturbances and how previous studies have differentiated between them.

Possible sources of event beds

The disturbance deposits in this record could be a result of floods, post-disturbance (wildfire, land-clearing, earthquake) erosion, or earthquakes. Because water is required to carry sediment, the post-disturbance erosional events are included with flooding. As a result, this study attempts to differentiate between within-lake disturbances (which could be local aseismic wall failures or earthquakes) and externally sourced (flood) deposits. Aseismic wall failures can then be differentiated from earthquake deposits by areal extent, where aseismic wall failures are more likely to be local and earthquake deposits are more likely to be found lake wide. Water transported (flood) deposits can be of two basic types based on the flood water density: 1) inter- or surface-flow deposits or 2) density current (turbidity or hyperpycnal flow) deposits.

Turbidites can be of many forms and can result from different types of extreme events, including earthquakes (e.g., Goldfinger et al., 2012; Morey et al., 2013; Howarth et al., 2014; Moernaut et al., 2014; Monecke et al., 2018; and Vandekerkhove et al., 2020) and floods (e.g., Wilhelm et al., 2012; Gilli et al., 2013; Wirth et al., 2013; Vandekerkhove et al., 2020). Earthquake-triggered deposits are typically mass-transport deposits (resulting from subaquatic landslides and debris flows) which form thick turbidites (Moernaut et al., 2014; Simmoneau et al., 2013), although smaller turbidites can result as well (Wilhelm et al., 2016; Moernaut et al., 2017; and Monecke et al. 2018). Floods usually last days to weeks and frequently produce deposits that reflect the waxing and waning of the flow which form inverse, then normally, graded deposits (Alexander and Mulder, 2002; St-Onge et al., 2004). In contrast, earthquake-triggered turbidites are typically normally graded deposits.

Does the record contain a disturbance deposited in 1700 CE?

Finding a disturbance deposit dated to 1700 CE in the sedimentary record from Lower Squaw Lake would be strong evidence that the lake records Cascadia earthquakes, however this is difficult to determine because of the challenges presented by the radiocarbon production curve (IntCal20; Reimer et al., 2020) over the past 300–400 years (Fig. 4). Variations in the radiocarbon production curve result in multiple intersections during radiocarbon calibration. The result is that there are multiple calendar ages that cannot be evaluated for their likelihood without additional information, as described in the Methods section. As previously mentioned, the radiocarbon samples are detrital and therefore may be older than the time of deposition (typically by decades to centuries; see, for example, Streig et al., 2020) because they resided in the watershed for an unknown amount of time prior to emplacement, and therefore must be considered maximum limiting ages.

Sample 2, taken from just below deposit J, produced a radiocarbon determination of 110 +/-25, similar to what would be expected for a sample that died around 1700 CE, however calibration of this sample results in three probability peaks. If we assume that the age of the samples represents the stratigraphic order in which they were deposited, there are two of these options for radiocarbon samples 1–4 with respect to the radiocarbon production curve that are younger than 1950. The third option (youngest calendar age distribution) is discounted because sample J was deposited prior to the inflection in sediment density that reflects a change in land use (logging and road building). Option 1 is the modeled distribution determined by the age-depth model (shown in Fig. 17, left), which places sample 2 at 1680–1780 and option 2 is an alternative which places sample 2 between 1800–1940 (Fig. 17, right). Constraining the upper portion of the record can be approached by using the sedimentation rates from nearby lakes. Given there are 71 cm of event-free sediment above deposit J and a sedimentation rate of ~ 1–3 cm/10 years (based on nearby Bolan Lake sedimentation rate; Briles et al., 2005, and the Upper Squaw Lake sedimentation rate; Colombaroli et al., 2018), the range of possible time represented between the time of collection and deposition at the location of sample 2 is between ~ 240–710 years. Using the average sedimentation rate from the age-depth model in Fig. 16 (~ 2 cm/10 yrs), the time represented by 71 cm is ~ 350 years. Because the radiocarbon age for this sample is 1680–1940 (unmodeled), the maximum age for deposit J is 1680 CE, which is ~ 330 years prior to the time of collection. This places the likely age of the sample between ~ 240–330 years prior to the date of collection, supporting an interpretation that the older of the calibration peak options (Fig. 17, left) is more likely.

Formation of deposit J at around the time of the 1700 CE earthquake is supported by additional information from Upper Squaw Lake. Colombaroli et al. (2018) used CT scans to estimate the proportion of fluvial silt at mm-resolution, then modeling an age-depth model using the silt-free sediment depths. Their method identified seven anomalously thick rapidly deposited layers (compared to a frequency-magnitude distribution) that were suspected to have been formed in response to a different process than flooding, possibly earthquakes. One of these thick events correlates to deposit J (see Fig. 12b). Their age-depth model resulted in an age range of 1718–1758 CE for this deposit, close to the maximum limiting radiocarbon age for deposit J, suggesting that the older part of the radiocarbon distribution is consistent with the sedimentation above the event, and the likelihood of stratigraphic order.

Replacing radiocarbon sample 2 with a calendar age of 1700 CE (blue lines indicating envelope boundaries shown in Fig. 16) produces model agreement statistics that support the assumption that deposit J is indeed at 1700 CE. For the original model with sample 2 results in moderate agreement between the data and model (overall agreement is 64.7%) whereas the model

using the 1700 CE date in place of sample 2 the agreement between the data and model are higher suggesting a better fit than obtained by the model with the radiocarbon sample 2 date ($A_{\text{comb}} = 0.8$ and 0.65 respectively).

Insight into depositional processes – XRF data

Distinctive patterns exist in the raw XRF data through the disturbance deposits (Figs. 14 and 15). To investigate these patterns, we represent the relationship between endmember indicators Ca and K (expressed as raw counts, after smoothing with a 9-point gaussian filter) for core SQB5 as a scatterplot in Fig. 18. Ca and K are useful elements for provenance tracing because Ca amphiboles (sourced primarily from the Slickear Creek drainage to Lower Squaw Lake from the north) are present in watershed rocks while K is more prevalent in muscovite (sourced from the Condrey Mountain Schist which provides material from Squaw Creek to Lower Squaw Lake; Table 7). No calcium rich rocks were detected in the Condrey Mountain Schist.

The scatterplot of the raw data (Fig. 18a) reveals patterns that were not obvious from the downcore representation of the elemental data (compare Fig. 18 to Figs. 14 and Fig. 15). A cartoon (Fig. 18b) illustrates that the original interpretation of the patterns in the raw data appear to reflect the relative amounts of each component with deposition (key to color coding for each disturbance A–J shown in Fig. 18c) through deposits. The XRF variables Ca and K expressed as peak area (raw counts), however, are not true endmember concentrations because the data contain artifacts. These artifacts are primarily related to bulk density (porosity) which affects the amount of material present in the X-ray beam and are different for each sample as a result of the “closed sum effect” (Rollinson, 1993; van der Weijden, 2002). A variety of factors, such as x-ray tube age, surface roughness, dilution by organic matter, and x-ray attenuation differences from variations in water content also contribute to these artifacts (Boyle et al., 2015; Löwemark et al., 2011; Thomson et al., 2006). To account for this, another variable is frequently used to normalize XRF elemental data to better quantify the composition of different components, at the expense of potentially adding analytical noise.

As a result, for comparison we normalized the raw data to silicon (Fig. 19a). This clearly shows that deposits J and H are enriched in calcium compared to other disturbance deposits. When scaled by CT density (Fig. 19b), the patterns in the scatterplot look very similar to that of the raw data. Because the raw data are highly reproduceable, and to first order the raw data represent the composition and density of the sediment, the raw data were chosen for this investigation, and are interpreted to reflect endmember composition changes with the implicit third variable, CT density. These loops, then, are interpreted to be representations of elemental changes with grading through deposits, where the XRF loops begin to deviate from the initial background value at the base of the deposit (identified by the encircled letters with subscript i in Fig. 18a). Note that deposit J is different from the others. This is described in detail in the following section.

Deposit J. Deposit J is a medium-silt deposit displaying unusual grading characteristics: it is well-sorted at the base (becoming less-so upward) and lacks diatoms and particulate and degraded organics present in the basal silt of many of the other disturbance event deposits. The base of the deposit is sharp, but there is evidence of loading into the organic-rich sediment below.

To gain insight into the processes influencing deposition, we look to the XRF geochemical data (Fig. 20). Note that the visible base and top of the deposit do not start and end at the background ratio. This gap (Fig. 20, top left) suggests that there is more at the base and top of the deposit than is visible by eye. In other words, the basal silt is preceded by, and followed by, sediment that is part of the disturbance deposit. This sediment (blue line, Fig. 20) suggests the preferential reduction in potassium (mica) prior the more obvious base of the silt which has a preferential initial increase in calcium (watershed sourced amphibole). Microscopic inspection identifies a thin micaceous silt layer followed by organic-rich sediment a few centimeters below the primary silt. Whereas this silt layer is indistinct in the northern cores, it is more obvious in the deeper water cores, especially SQB9. This suggests that the precursor is a small bypass turbidite (fine-grained turbidites that are formed when the coarser sediment bypasses the location; Bouma, 2000) that is visibly present in deeper water cores but indistinct in the northern shallower water cores.

Sediment above the primary silt unit (green line, Fig. 20) suggests a long tail deposit that returns to the initial position with respect to the background ratio. This tail is also visible in the CT density. The tail is followed by a very low CT density (a few cm thick) that appears to be part of the background sediment; however, the diatoms and other water column organisms are of different species (see smear slides in Fig. 11). The XRF data suggests that grading through the deposit is complex. As grading progresses upward, the XRF pattern changes in way that appears to reflect the partitioning of entrained background sediment into components slightly enriched in each elemental endmember: as the deposit grades upward, first in the direction of Ca, then returning to background slightly depleted in Ca (or enriched in potassium). The presence of this tail is supported by the loss on ignition data that shows a 30% decrease in inorganic content along the length of the tail.

The XRF data from the base of the silt upward through the tail is more complex compared to the other deposits. This variability is unlikely to reflect multiple events through time because values don't ever go back to background. This supports the interpretation that this is a single deposit that formed as a result of an energetic event that partitioned particles in the water column during settling, and not the result of post-earthquake watershed removal of sediment through time.

Deposits H and I. Deposits H and I form a complex sequence that settled between 1819–1875 CE (based on the age-depth model). A thin layer of deciduous leaves between deposits H and I suggests deposit I had time to settle (minutes to weeks), but not enough time for interevent sediment to accumulate. We describe them below in order of deposition because they appear to have formed in response to the same event or two very closely spaced events.

Deposit I is a turbidite composed of disaggregated schist with visible mica fragments. It displays reversed, then normal grading from a medium-grained silt upward to form a short organic tail followed by a thin layer of deciduous leaves (forming the boundary between the schist turbidite and the silt from deposit H above). Deposit I is very similar to deposit E, a local lake-margin slope-failure deposit, in that it is a turbidite formed of dark gray schist with large mica flakes. It contrasts with deposit E in that it is found in all cores, suggesting that deposit I was formed as a result of a lake-wide disturbance that was strong enough to create a synchronously triggered mass-transport deposit composed of lake-margin schist. This disturbance is suspected to be the result of the 1873 CE Brookings earthquake because shaking was strong enough in this region to cause chimneys to topple.

In contrast, deposit H is composed of watershed-sourced sediment in core SQB2 and SQB5 (more so than any other deposit based on XRF; Fig. 15). The deposit appears to have a long tail in SQB2 (Fig. 21), but it is hummocky with respect to CT density instead of smoothly grading upward. SQB9, from the lake's depocenter, contains a temporally correlative to deposit H, but it is composed of multiple turbidites (Fig. 21). This deposit is similar to Deposit G in that in both cases the northern cores contain sediment with a higher silt content compared to background, while SQB9 contains turbidites (see Fig. 21). Deposit H contrasts with deposit G in having a distinctive basal silt and tail deposit composed primarily of sediment sourced from the watershed.

The multiple units in deposit H in deep-water core SQB9 have several possible explanations: (a) they could represent synchronously triggered "amalgamated turbidites" (using the terminology of Van Daele et al., 2017, p. 77–78), suggesting individual subaqueous landslides traveled different distances to reach the lake's depocenter (SQB9), (b) "turbidite stacks" (again, using the terminology Van Daele et al., 2017, p. 77–78) suggesting triggers closely spaced, but not synchronous, events in time, (c) they could be the result of reflection waves or a seiche, (d) a mainshock and aftershock sequence for a proximal earthquake; (e) an earthquake with a complex source function, or (f) a retrogressive failure sequence after an earthquake.

Mechanism (a) is possible, however there is only one main channel system and therefore it is unlikely that these are the result of separate subaqueous landslides around the lake. Mechanisms (b) and (d) are unlikely because the deposits are less likely to have been deposited over some time (longer than days) because the XRF scatterplot through deposit H in core SQB5 is a continuous loop (which does not go back to background until the end; Fig. 22). This suggests a single event, with aftershocks, which can sometimes be immediate and continuous for hours after the mainshock (such as with the 2011 Tohoku earthquake; Toda and Stein, 2018), although the 1873 Brookings earthquake was determined to be the result of an

in slab event because no aftershocks were felt. Mechanism (e) is unlikely because a complicated source function for the same reason: there are no descriptions of a complex shaking pattern. The most likely (and simplest explanation) is that the landslide dam failed triggering deposit, then retrogressive failures of the landslide occurred while sustained shaking caused deposit H to form until stability was reached when shaking ceased. Although this scenario seems plausible, there is no definitive evidence to support it.

In summary, we suggest the following sequence to explain deposits H and I. An initial earthquake caused the landslide dam to fail, resulting in the partial draining of the lake and the formation of the lake-wide slope failure deposit composed of weathered schist which settled to form deposit I. Shaking resulted in retrogressive failure of the landslide dam and cyclic loading and liquefaction of the lake's delta, releasing sediment and groundwater into the lake mid-depth which settled to form deposit H.

Deposit G. Deposit G, based on the age-depth model, settled between 1827–1892 CE. It is indistinct in SQB2, appearing slightly denser than background sediment, with maximum density at the deposit center. The composition remains mixed (Fig. 15) with changes in density throughout the deposit, but the slope is relatively flat toward K (relative to the slope of background sediment), similar to (but not as extreme as) deposit E. This deposit in SQB2 is similar to the waxing and waning flood deposit reported by St-Onge et al. (2004), who analyzed a sedimentary sequence from Saguenay Fjord, Québec, that was produced from a known historic earthquake followed by a flood (which was the result of a landslide dam breach). The age-depth model suggests that Deposit G could be the result of the dam failure in 1881, the 1873 Brookings earthquake, or the flood of 1861-62. The installation of the dam is unlikely to have caused this deposit because the dam is located in the south, far from SQB2. The 1873 Brookings earthquake caused severe shaking in the region (Ellsworth, 1990) and therefore is more likely to have caused large disturbance deposits H or I (see discussion above) and not deposit G. The proximity of the sample to the inflection in sediment density suggests a timing close to when the dam was installed, and land use changes occurred. Based on timing, it is suggested that this is the result of the dam failure in 1881 CE.

This interpretation is supported by the presence of the sequence of disturbances in SQB9 located near the lake's depocenter (Fig. 21). There are three possible explanations for these amalgamated deposits: either they were 1) formed as a result of several wall failures with differential travel times, 2) they are reflection deposits from a small seiche in response to the dam failure, or 3) they are the result of retrogressive landslides in response to destabilization of the landslide toe when the built dam failed. Because the lake is small with only one main channel and the formation of a seiche in response to the dam failure unlikely, we propose that the sequence is the result of a retrogressive failure sequence from repeated destabilization of the landslide toe when the dam failed until the landslide stabilized. We conclude that this deposit formed in response to the flood and associated dam failure in 1881 CE and adjustments of the landslide in response to the dam failure.

Deposit F. Deposit F is a simple graded deposit which the age-depth model suggests settled between 1835–1908 CE. This deposit shows evidence of loading onto the organic sediment below in SQB2. The mineralogic composition is unknown, however the XRF data suggests a mixed composition enriched in K that does not vary with changes in density at the midpoint of the deposit. Lower Squaw Lake was influenced by a sequence of closely spaced events that began with the 1861–1862 event. These include the failure of the dam as the result of the 1861–1862 atmospheric river event, the 1873 Brookings earthquake, the installation of the dam in 1877, the winter rain-on-snow event in 1881 (which caused the newly installed dam to fail), a large flood in 1890 (#2 of 3 based on stream gage data), and a smaller flood in 1892. Given that the 1890 flood is the largest in this set, it seems possible that Deposit F is the result of the flood of 1890, although it could be the result of an unidentified earthquake observed in offshore Trinidad cores dated to ~ 1830's (Goldfinger et al., 2019).

Deposit E. This deposit is only found in core SQB5, which is located on a steep slope. There is no age data for this deposit because it cannot definitively be identified in the chronology core SQBss/1/2 composite, however the time of deposition is between deposits D and F. Deposit E is predominantly composed of Condrey Mountain Schist (based on XRD and the dark gray color of the deposit with visible mica flakes). The XRF data shows that changes through the deposit goes primarily in the direction of K, implying a relative increase in mica concentration. Slope failures are common at the location of SQB5, indicated by the large amount of sediment missing between deposits B and J in the short cores identified as narrow and wide diameter

short cores (see false color image of core density at the top left of Fig. 12a). This deposit was likely the result of a local lake-margin wall failure because it is found in only one core, and the mica composition suggests a lake-margin bedrock source for the sediment (not a mixed source as would be expected from the disturbance of surficial sediment). An aseismic local wall-failure deposit could have resulted from heavy winter rains (similar to the deep-seated slope failure that occurred in response to heavy rains during the winter of 2016). Alternatively, it is possible that deposit E is a local wall failure that resulted from an earthquake.

Deposit D. The age-depth model suggests that deposit D settled between 1870–1940 CE. Deposit D is indistinct and unusual in many ways. It is a sequence of three silt units (the lower-most is thickest and visually obvious) within a stiff layer of organic-rich silt (in SQB2). This deposit has a small counterclockwise loop in XRF (Fig. 15) and the lower silt unit is a simple graded unit. This basal silt is orange in color and is fine-grained and well-sorted. The XRF and XRD data suggest that although the majority of the deposit is of mixed composition, with preferential enrichment of watershed-sourced sediment at the deposit base. This could be the result of an interflow flood deposit containing watershed-sourced sediment. It is unlikely to be the result of the 1873 Brookings earthquake because regional shaking was strong and deposit D is indistinct (except for the thin layer of orange silt at the base).

The age-depth model suggests that deposit D may be the result of flood events or the 1906 San Andreas earthquake. Given that there are 58 cm (event-free) over the past 126 years (based on the location of the inflection in sediment density), and there are 14 cm between this inflection and deposit D, this makes the age of deposit D: the date of inflection (~ 1850 to ~ 1880) + 30 years = 1880 to 1910 CE. This is very close to the time of the 1906 CE San Andreas earthquake or the 1890 flood. The presence of a disturbance event deposit from the 1906 CE San Andreas earthquake seems plausible because felt reports from the region suggest MMI values of ~ IV in this region (Dengler, 2008). The results, however, are inconclusive.

Deposit C. The age-depth model suggests deposit C settled between 1880–1950 CE. Deposit C is a normally graded unit with an unknown composition that becomes thinner with distance from Squaw Creek (see below deposits A and B in Fig. 6), suggesting it is the result of a flood. The most likely events to produce this deposit (based on the size of the event) are the third largest flood of five (which occurred in 1955) or the flood in 1927 associated with a debris dam failure. Given that the average sedimentation rate is ~ 2.5 year/cm and the interevent sediment thickness between Deposits B and C is 18 cm (after accounting for erosion; top left Fig. 8), it is most likely that deposit C is the result of the 1927 flood with debris dam failure, however this remains uncertain because the sedimentation rate is highly variable in the lake. No sediment provenance data exists for this deposit; however, in core SQB5, this deposit is brown in color, similar to the lower halves of Deposits A and B. Although outside the time range, there is the possibility that it could be the result of the large flood in 1955 CE or the atmospheric river event in 1861-62 CE. The 1861-62 flood is considered unlikely, however, because deposit C was deposited well after the inflection point in CT density that is suggested to be the result of land use changes in the mid-late 1800's.

Deposits A and B. Deposits A (deposited between 1980–2013 CE) and B (attributed to the 1964 flood based on comparison to Upper Squaw Lake) are 5–20 cm thick, depending on location in the lake, with lake-wide extent and similar characteristics (Fig. 6). They have sharp bases with sediment likely missing below in all cores other than the deepest water cores (SQB9 and SQB10), contain basal sediment with rootlets and degraded organic matter, and are coarse-grained, normally graded deposits. These characteristics suggest they are the result of erosive turbidity currents. Although the deposits are quite similar to one another, the base of deposit A (which is incomplete in core SQB5) is composed of calcium-rich coarse silt at the base, whereas the base of deposit B is composed of potassium-rich coarse micaceous silt.

Deposits A and B were most likely deposited in response to large flood events because the most recent events are the two largest flood events that occurred in 1997 and 1964, except for the drainage of the lake for dam maintenance in 1972. Multiple first-hand reports describe the nature of the extreme flood of 1997 in the vicinity of Lower Squaw Lake: A landowner described the flood as having transported watershed-sourced beach sand from one end of the lake to the other (B. Harr; June 2015), and U. S. Forest Service employees (personal communication, P. Jones; December 2019; J. McKelligott, December 2020) described debris caught at the dam that caused the lake level to rise a few feet above the maximum water level. Water was seen shooting 10 feet out of the spillway and caused damage to the gate. At Applegate Reservoir, a few kilometers downstream

from Squaw Lakes, water was flowing over the earthen dam and observed to undercut surficial slope sediment, causing slumping into the reservoir (P. Jones, personal communication, December 2019). The extreme nature of this flood, relative timing compared to the 1964 flood and observations of beach sand suggest that the 1997 flood produced deposit A, the uppermost deposit in the record. There were no other disturbance events around this time. Because there are no other disturbance deposits with similar characteristics downcore, these events were either more extreme than in the past, or the supply of readily mobilized sediment has increased (which is likely given logging contributions to sediment). It is also possible that the built dam is more likely to trap debris and elevate the lake level in response to extreme flooding than the natural landslide dam.

Organic-rich tail deposits

The most likely earthquake deposits are the sequence formed by deposits H and deposit J. These have the following similar characteristics:

1. They appear to have tails enriched in watershed-sourced sediment displaying organic grading
2. The grain size distributions from the silt upward into the tail contains a dominant medium silt and a smaller percentage of finer-grained (fine silt and clay) particles.
3. The tail is followed by normal background sedimentation that has very low density and contains a different composition and size of water column organisms.

We hypothesize these organic-rich tails and the post-deposition change in community structure may be diagnostic of earthquake-triggered deposits because it is a characteristic of deposits H and J. To understand their structure more fully, we used regression to describe the relationship between CT density and inorganic content (Fig. 24a) using data from SQB1/2 (and surface sample) and SQB14 to determine if the tail deposits display organic grading. To do this, we estimated the inorganic content of the sediment from the measured CT density data using the equation:

$$\% \text{ INORG} = -2518 \cdot \text{CT} + 98.695 \text{ (which explains 97\% of the variance).}$$

The regression explains 97% of variance. The residuals demonstrate that the correlation between organic content and CT density data is very high for CT values greater than 300 HU but deviate from the relationship below this. We suspect that the correlation breaks down due to imperfect registration between LOI and CT density data, or because % calcium carbonate was not included with the inorganic content data. We used this equation to estimate the percentage of inorganic content in core SQB5 (Fig. 24). This figure clearly shows a reduction in inorganic content upward from the denser silt layers for deposits H and J.

It is suspected that the source of the watershed-sourced silt in both deposit J and H is the result of liquefaction of the lake's large delta. Sediment loading the lake margin in the north is of mixed composition and therefore shallow slope failures are likely to be composed of the same mixed composition. Slicear Creek transports water aboveground until it reaches the upper reach of the delta, then flows as groundwater to the lake through the coarse-grained delta deposit. The deltaic sediment comprises a wide size range of particles, from gravel to sand, formed by flash floods, and as a result is stratified to some degree. It is suspected that liquefaction or settling of the delta matrix causes the release of fine particles from the delta to explain the watershed composition of deposits J and H.

Inferred sequence in response to sustained, not necessarily strong, ground motion

In summary, we suggest the following scenario to explain the sedimentological, physical, and geochemical properties observed in Deposit J (Fig. 25). Initial shaking disturbed lake-margin sediments, generating a small turbidite, which bypassed SQB2. Subsequent sustained ground motion caused liquefaction or the release of fluids from the lakes' large, subaerial delta, forcing fine particles and groundwater out from its coarse-grained matrix. This resulted in the release of watershed-sourced sediment into the lake near the thermocline (similar to an interflow) where the denser silt settled out of the water column first while the platy mica grains remained in suspension longer due to a combination of surface area, density, and turbulence from

a possible internal wave. As shaking slowed, the mica-rich schist sediment would begin to settle out of suspension. These events may have caused the water column to become stripped of organic matter with diatoms and fine sediment trapped in it, possibly resulting in a collapse of (or at least change in) the lake ecosystem.

Interpretations: attribution of deposits to historic events

Here we present a summary of each of the deposits A–J, their characteristics and attributions. There appear to be three types of flood deposits. The first type is represented by deposits A and B. They are thick turbidites with high magnetic susceptibility and density, but with a lower magnetic susceptibility in the lower half which is brown in color from the organic matter entrained in the base. These show evidence of erosion. The second type of flood deposit is an interflow deposit which is a simple graded silt unit exemplified by deposit C. This unit has a wavy discontinuous base in the northern cores and is thicker to the south. The third type of flood deposit is represented by deposit G which displays reverse then normal grading.

Three types of earthquake deposits are suggested by the data. The first type is represented by deposit J. Deposit J is a complex sequence with an initial bypass turbidite followed by a watershed-sourced silt and a long, organic-rich tail. The second type of earthquake deposit, represented by deposits H and I, is also complex with an initial thick turbidite sourced from the schist and followed by a watershed-sourced silt and a long, organic-rich tail. The third type of earthquake deposit suggested by the data is a simple graded turbidite deposit, represented by deposit D and possibly F. The silt units show evidence of loading on the organic sediment below.

Conclusions

The setting at Lower Squaw Lake, Oregon, (~ 180 km inland of the deformation front in Cascadia) provided a unique opportunity to determine how seismically generated disturbance deposits can be differentiated by elemental and grain-size structure from deposits from other types of disturbances, such as floods. Based on these results, disturbance types can be differentiated as follows:

Flood deposits. Flood deposits are highly variable in character, however all have counterclockwise XRF grading patterns. Extreme floods with high water produce thick turbidites like deposits A and B, with erosive bases containing organic matter and a thin silty-clay cap. Possible interflow floods produce simple graded deposits similar to deposit F. Flooding with a dam failure results in disturbances like deposit G, with a simple reverse then normal grading in shallow water cores, but multiple disturbances (possibly retrogressive landslide failures in response to destabilization of the landslide at the toe due to the landslide dam failure) in deep water cores.

Earthquake deposits. Earthquake deposits identified in this study are of the following types. The deposit suspected to be the result of the 1700 CE Cascadia earthquake is a complex sequence with an initial faintly expressed turbidite followed by a watershed-sourced silt with load structures at the base. This silt is very well-sorted and pure at the base, then grades upward into a long, organic-rich tail. The deposit suspected to result from the 1873 CE Brookings earthquake is also complex but has a lake-wide wall-failure turbidite at the base followed by a watershed sourced silt, similar to that of the 1700 CE Cascadia earthquake. This deposit is different in that there are multiple deposits in the deep-water cores, similar to deposit G that included the failure of the landslide dam.

We conclude that it is possible to distinguish crustal and plate boundary earthquakes, and from flood deposits, using the sedimentological characteristics and sediment provenance data at Lower Squaw Lake.

Declarations

ACKNOWLEDGMENTS

This research was partially supported by the National Earthquake Hazards Reduction Program of the U.S. Geological Survey (through a grant to Andrew Meigs and Simon Engelhart, USGS Grant G17AP00028). The USGS Earthquake Hazards Program

through Alan R. Nelson (USGS, Golden) partially supported the collection of some Livingstone cores and CT scans of Livingstone and Kullenberg cores. Geological Society of America awards provided additional funding: a graduate student research grant and the Kerry Kelts Limnogeology Award. Coring in 2015 would not have been possible without contributions from Joseph Stoner, Roy Haggerty, and a donation from Ruth Morey.

The US Forest Service granted permission for this study (special thanks go to Starr Ranger Station employees and the regional office in Grants Pass, OR). We are extremely grateful for the assistance and knowledge provided by Ranger John McKelligott, and for field assistance by Mark Anthony (USFS employee who participated in coring in 2015). Bert Harr generously allowed access to his Slickear Creek property during this investigation and contributed significantly to this project through his vast knowledge of local extreme events and local and regional history since 1900. Peter Jones provided personal historic accounts of the more recent historic floods.

This project could not have happened without the generous assistance from numerous volunteers. Katie Alexander (Western Washington University) spent a few days canoeing in the cold to acquire bathymetric data. Maureen Walczak (OSU) generously analyzed my first radiocarbon samples and provided guidance on how to use the radiocarbon production curve to select samples. Jamie Howarth (then at GNS, NZ) provided useful coring information and guidance, including sharing his approach to dating an earthquake event in lake sediments from about the same time as the 1700 CE Cascadia earthquake. Other volunteer field assistants included Randy Keller, Brendan Reilly, Katie Alexander, and many others. Christy Briles (Colorado University, Denver) helped train me in the fine art of lake coring during a fateful summer week in 2010.

LacCore and the University of Minnesota, provided Kullenberg coring equipment and expertise. Thanks also go to the OSU core repository (especially Maziet Cheseby) for housing cores and providing the tools to process them. Carol Chin aided core processing of the Kullenberg cores, for which we are extremely grateful. We would like to thank Anders Carlson for allowing me to be one of the first users of the Itrax. Finally, AEM would like to thank her committee and other key advisors, including Joseph Stoner, Eric Kirby, Alan C. Mix, Jason R. Patton, Maarten Van Daele, Lonnie Leithold, Karl Wegmann, Joseph D. Ortiz, and Nicklas G. Piasias for discussions and guidance.

NOTE: The authors declare no conflicts of interest.

References

- Alexander, J., & Mulder, T. (2002). Experimental quasi-steady density currents. *Marine Geology*, 186(3-4), 195-210.
- Bakun, W. H. (2000). Seismicity of California's north coast. *Bulletin of the Seismological Society of America*, 90(4), 797–812. <https://doi.org/10.1785/0119990138>
- Beck, C. (2009). Late quaternary lacustrine paleo-seismic archives in north-western Alps: Examples of earthquake-origin assessment of sedimentary disturbances. *Earth-Science Reviews*, 96(4), 327–344. <https://doi.org/10.1016/j.earscirev.200907.005>
- Bouma, A. H. (2000). Coarse-grained and fine-grained turbidite systems as end member models: applicability and dangers. *Marine and Petroleum Geology*, 17(2), 137-143.
- Boyle, J. F., Chiverrell, R. C., & Schillereff, D. (2015). Approaches to water content correction and calibration for μ XRF core scanning: Comparing X-ray scattering with simple regression of elemental concentrations. In I. W. Croudace, & R. G. Rothwell (Eds.), *Micro-XRF studies of sediment cores* (pp. 373–390). Springer.
- Bradbury, J. P. (1996). Charcoal deposition and redeposition in Elk Lake, Minnesota, USA. *The Holocene*, 6(3), 339-344.
- Briles, C. E., Whitlock, C., & Bartlein, P. J. (2005). Postglacial vegetation, fire, & climate history of the Siskiyou Mountains, Oregon, USA. *Quaternary Research*, 64(1), 44–56. <https://doi.org/10.1016/j.yqres.2005.03.001>

- Brocher, T. M. (2020). Was the 23 November 1873 California-Oregon border earthquake, USA, an inslab earthquake? U.S. Geological Survey Open-File Report 201x-xxxx, <https://doi.org/10.3133/ofr2017xxxx>
- Bronk Ramsey, C., (2017). *OxCal Program* (Version 4.3.2) [Computer software]. Oxford University Research Lab for Archaeology. <https://c14.arch.ox.ac.uk/oxcal.html>
- Campbell, C. (1998). Late Holocene lake sedimentology and climate change in southern Alberta, Canada. *Quaternary Research*, 49(1), 96–101. <https://doi.org/10.1006/qres.1997.1946>
- Coleman, R. G., Helper, M. D., & Donato, M. M. (1983). *Geologic map of the Condrey Mountain roadless area, Siskiyou County, California*. U.S. Geological Survey Miscellaneous Field Studies Map MF-1549A.
- Colombaroli, D., & Gavin, D. G. (2010). Highly episodic fire and erosion regime over the past 2,000 y in the Siskiyou Mountains, Oregon. *Proceedings of the National Academy of Sciences*, 107(44), 18909–18914. <https://doi.org/10.1073/pnas.1007692107>
- Colombaroli, D., Gavin, D. G., Morey, A. E., & Thorndycraft, V. R. (2018). High resolution lake sediment record reveals self-organized criticality in erosion processes regulated by internal feedbacks. *Earth Surface Processes and Landforms*, 43(10), 2181–2192. <https://doi.org/10.1002/esp.4383>
- Donato, M. M. (1993). Preliminary geologic map of the Squaw Lakes quadrangle, Oregon and California (No. 93-703).
- Ellsworth, W. L. (1990). Earthquake history, 1769–1989. In R. E. Wallace (Ed.), *The San Andreas fault system, California* (pp. 152–187). U.S. Geological Survey.
- Engstrom, W. N. (1996). The California storm of January 1862. *Quaternary Research*, 46(2), 141–148. <https://doi.org/10.1006/pres.1996.0054>
- Gilli, A., Anselmetti, F. S., Glur, L., & Wirth, S. B. (2013). Lake Sediments as Archives of Recurrence Rates and Intensities of Past Flood Events. In M. Schneuwly-Bollschweiler, M. Stoffel & F. Rudolf-Miklau (Eds.), *Dating torrential processes on fans and cones* (vol. 47, pp. 225–242). Springer.
- Goldenson, N., Leung, L. R., Bitz, C. M., & Blanchard-Wrigglesworth, E. (2018). Influence of Atmospheric Rivers on Mountain Snowpack in the Western United States. *Journal of Climate*, 31(24), 9921–9940.
- Goldfinger, C., Galer, S., Beeson, J., Hamilton, T., Black, B., Romsos, C., Patton, J., Nelson, C. H., Hausmann, R., & Morey, A. (2017). The importance of site selection, sediment supply, and hydrodynamics: A case study of submarine paleoseismology on the northern Cascadia margin, Washington USA. *Marine Geology*, 384, 4–16, 17, 25–46. <https://doi.org/10.1016/j.margeo.2016.06.008>
- Goldfinger, C., Grijalva, K., Bürgmann, R., Morey, A. E., Johnson, J. E., Nelson, C. H., Gutiérrez-Pastor, J., Ericsson, A., Karabanov, E., Chaytor, J. D., Patton, J., & Gràcia, E., (2008). Late Holocene rupture of the northern San Andreas fault and possible stress linkage to the Cascadia subduction zone. *Bulletin of the Seismological Society of America*, 98(2), 861–889. [.org/0.1785/0120060411](https://doi.org/10.1785/0120060411).
- Goldfinger, C., & Gutierrez, J. (2019). Possible stratigraphic evidence of stress triggering of the northern San Andreas fault following southern Cascadia earthquakes. *Proceedings of the American Geophysical Union* (pp. OS54A-03). San Francisco, CA, US.
- Goldfinger, C., Morey, A. E., Black, B., Beeson, J., Nelson, C. H., & Patton, J. (2013). Spatially limited mud turbidites on the Cascadia margin: Segmented earthquake ruptures? *Natural Hazards and Earth System Sciences*, 13(8), 2109–2146. <https://doi.org/10.5194/nhess-13-2109-2013>

- Goldfinger, C., Nelson, C. H., Morey, A. E., Johnson, J. E., Patton, J. R., Karabanov, E. B., Gutierrez-Pastor, J., Eriksson, A. T., Gràcia, E., Dunhill, G., Enkin, R. J., Dallimore, A., & Vallier, T. (2012). *Turbidite event history: Methods and implications for Holocene paleoseismicity of the Cascadia subduction zone* (US Geological Survey Professional Paper 1661-F). <https://doi.org/10.3133/pp1661F>
- Hennebelle, A., Aleman, J. C., Ali, A. A., Bergeron, Y., Carcaillet, C., Grondin, P., ... & Blarquez, O. (2020). The reconstruction of burned area and fire severity using charcoal from boreal lake sediments. *The Holocene*, 30(10), 1400-1409.
- Horton, D. E., Johnson, N. C., Singh, D., Swain, D. L., Rajaratnam, B., & Diffenbaugh, N. S. (2015). Contribution of changes in atmospheric circulation patterns to extreme temperature trends. *Nature*, 522(7557), 465–469. <https://doi.org/10.1038/nature14550>
- Hotz, P. E. (1979). *Regional metamorphism in the Condrey Mountain quadrangle, north-central Klamath Mountains, California* (Geological Survey Professional Paper No. 1086). U.S. Government Printing Office.
- Howarth, J. D., Fitzsimons, S. J., Norris, R. J., & Jacobsen, G. E. (2012). Lake sediments record cycles of sediment flux driven by large earthquakes on the Alpine fault, New Zealand. *Geology*, 40(12), 1091–1094. <https://doi.org/10.1130/G33486.1>
- Howarth, J. D., Fitzsimons, S. J., Norris, R. J., & Jacobsen, G. E. (2014). Lake sediments record high intensity shaking that provides insight into the location and rupture length of large earthquakes on the Alpine Fault, New Zealand. *Earth and Planetary Science Letters*, 403, 340-351.
- Inouchi, Y., Kinugasa, Y., Kumon, F., Nakano, S., Yasumatsu, S., & Shiki, T. (1996). Turbidites as records of intense palaeoearthquakes in Lake Biwa, Japan, *Sedimentary Geology*, 104(1–4), 117–125. [https://doi.org/10.1016/0037-0738\(95\)00124-7](https://doi.org/10.1016/0037-0738(95)00124-7)
- Johnson, D. M. (1985). *Atlas of Oregon Lakes*. Oregon State University Press.
- Karlin, R. E., & Abella, S. E. (1992). Paleoearthquakes in the Puget Sound region recorded in sediments from Lake Washington, USA. *Science*, 258(5088), 1617–1620. <https://doi.org/10.1126/science.258.5088.1617>
- Karlin, R. E., & Abella, S. E. B. (1996). A history of Pacific Northwest earthquakes recorded in Holocene sediments from Lake Washington. *Journal of Geophysical Research Solid Earth*, 101(B3), 6137–6150. <https://doi.org/10.1029/95JB01626>
- Karlin, R. E., Holmes, M., Abella, S. E. B., Sylwester, R. (2004). Holocene landslides and a 3500-year record of Pacific Northwest earthquakes from sediments in Lake Washington. *Geological Society of America Bulletin*, 116(1), 94–108. <https://doi.org/10.1130/B25158.1>
- Karlin, R., & Seitz, G. (2007). *A basin wide record of earthquakes at Lake Tahoe: Validation of the earthquake induced turbidite model with sediment core analysis: Collaborative research with UNR and SDSU*. Final Technical Report for 07HQGR0014 and 07HQGR0008, 18 pp.
- Kelts, K., Briegel, U., Ghilardi, K., & Hsu, K. (1986). The limnogeology-ETH coring system. *Swiss Journal of Hydrology*, 48(1), 104–115. <https://doi.org/10.1007/BF02544119>
- Kneller, B. C., & McCaffrey, W. D. (2003). The interpretation of vertical sequences in turbidite beds: The influence of longitudinal flow structure. *Journal of Sedimentary Research*, 73(5), 706–713. <https://doi.org/10.1306/031103730706>
- LaLande, J., 1995. An environmental history of the Little Applegate River watershed. USDA, Forest Service, Medford, OR. Website <http://soda.sou.edu/awdata/020912c1.pdf> (accessed 12 February 2014).
- Lamoureux, S. (2002). Temporal patterns of suspended sediment yield following moderate to extreme hydrological events recorded in varved lacustrine sediments. *Earth Surface Processes and Landform*, 27(10), 1107–1124.

<https://doi.org/10.1002/esp.399>

Larson, D.W. (1975). *Preliminary Investigation of Mercury in Squaw Lakes, Applegate River Basin, Oregon*. US Army Corps of Engineers, Portland District.

Leithold, E. L., Wegmann, K. W., Bohnenstiehl, D. R., Smith, S. G., Noren, A., & O'Grady, R. (2018). Slope failures within and upstream of Lake Quinault, Washington, as uneven responses to Holocene earthquakes along the Cascadia subduction zone. *Quaternary Research*, *89*(1), 178–200. <https://doi.org/10.1017/qua.2017.96>

Leithold, E. L., Wegmann, K. W., Bohnenstiehl, D. R., Joyner, C. N., & Pollen, A. F. (2019). Repeated megaturbidite deposition in Lake Crescent, Washington, USA, triggered by Holocene ruptures of the Lake Creek-Boundary Creek fault system. *GSA Bulletin*, *131*(11-12), 2039-2055.

Long, C. J., Whitlock, C., Bartlein, P. J., & Millspaugh, S. H. (1998). A 9000-year fire history from the Oregon Coast Range, based on a high-resolution charcoal study. *Canadian Journal of Forest Research*, *28*(5), 774–787. <https://doi.org/10.1139/x98-051>

Löwemark, L., Chen, H. F., Yang, T. N., Kylander, M., Yu, E. F., Hsu, Y. W., Lee, T. Q., Song, S. R., & Jarvis, S. (2011). Normalizing XRF-scanner data: A cautionary note on the interpretation of high-resolution records from organic-rich lakes. *Journal of Asian Earth Sciences*, *40*(6), 1250–1256. <https://doi.org/10.1016/j.jseaes.2010.06.002>

McCrorry, P. A., Hyndman, R. D., & Blair, J. L. (2014). Relationship between the Cascadia fore-arc mantle wedge, nonvolcanic tremor, and the downdip limit of seismogenic rupture. *Geochemistry, Geophysics, Geosystems*, *15*(4), 1071–1095. <https://doi.org/10.1002/2013GC005144>

Moernaut, J., Van Daele, M., Heirman, K., Fontijn, K., Strasser, M., Pino, M., ... & De Batist, M. (2014). Lacustrine turbidites as a tool for quantitative earthquake reconstruction: New evidence for a variable rupture mode in south central Chile. *Journal of Geophysical Research: Solid Earth*, *119*(3), 1607-1633.

Moernaut, J., van Daele, M., Strasser, M., Clare, M. A., Heirman, K., Viel, M., Cardenas, J., Kilian, R., de Guevara, B. L., Pino, M., Urrutia, R., & De Batist, M. (2017). Lacustrine turbidites produced by surficial slope sediment remobilization: A mechanism for continuous and sensitive turbidite paleoseismic records. *Marine Geology*, *384*, 159–176. <https://hdl.handle.net/10.1016/j.margeo.2015.10.009>

Moernaut, J., De Batist, M., Charlet, F., Heirman, K., Chapron, E., Pino, M., ... & Urrutia, R. (2007). Giant earthquakes in South-Central Chile revealed by Holocene mass-wasting events in Lake Puyehue. *Sedimentary Geology*, *195*(3-4), 239-256.

Monecke, K., Anselmetti, F. S., Becker, A., Sturm, M., & Giardini, D. (2004). The record of historic earthquakes in lake sediments of Central Switzerland. *Tectonophysics*, *394*(1–2), 21–40. <https://doi.org/10.1016/j.tecto.2004.07.053>

Monecke, K., McCarthy, F. G., Hubeny, J. B., Ebel, J. E., Brabander, D. J., Kielb, S., ... & Pentesco, J. (2018). The 1755 Cape Ann earthquake recorded in lake sediments of eastern New England: An interdisciplinary paleoseismic approach. *Seismological Research Letters*, *89*(3), 1212-1222.

Morey, A. E., Goldfinger, C., Briles, C. E., Gavin, D. G., Colombaroli, D., & Kusler, J. E. (2013). Are great Cascadia earthquakes recorded in the sedimentary records from small forearc lakes? *Natural Hazards and Earth System Sciences*, *13*, 2441–2463. <https://doi.org/10.5194/nhess-13-2441-2013>

Mulder, T., Syvitski, J. P. M., Migeon, S., Faugeres, J. C., & Savoye, B. (2003). Marine hyperpycnal flows; initiation, behavior and related deposits; a review: Turbidites; models and problems. *Marine and Petroleum Geology*, *20*(6), 861–882. <https://doi.org/10.1016/j.marpetgeo.2003.01.003>

Patton, J. R., Goldfinger, C., Morey, A. E., Ikehara, K., Romsos, C., Stoner, J., Djadjadihardja, Y., Ardhyastuti, S., Gaffar, E. Z., & Vizcaino, A. (2015). A 6600 year earthquake history in the region of the 2004 Sumatra-Andaman subduction zone earthquake.

- Praet, N., Moernaut, J., van Daele, M., Boes, E., Haeussler, P. J., Strupler, M., Schmidt, S., Loso, M. G., & De Batist, M. (2017). Paleoseismic potential of sublacustrine landslide records in a high-seismicity setting (south-central Alaska). *Marine Geology*, 384, 103–119. <https://lib.ugent.be/catalog/pug01:8527689>
- Reimer, P. J., Bard, E., Bayliss, A., Beck, J. W., Blackwell, P. G., Ramsey, C. B., Buck, C. E., Cheng, H., Edwards, R. L., Friedrich, M., Grootes, P. M., Guilderson, T., Hafliðason, H., Hajdas, I., Hatté, C., Heaton, T., Hoffmann, D. L., Hogg, A. G., Hughen, K. A., ... van der Plicht, J. (2013). IntCal13 and marine13 radiocarbon age calibration curves 0–50,000 years cal BP. *Radiocarbon*, 55(4), 1869–1887. https://doi.org/10.2458/azu_js_rc.55.16947
- Reimer, P. J., Austin, W. E., Bard, E., Bayliss, A., Blackwell, P. G., Ramsey, C. B., ... & Talamo, S. (2020). The IntCal20 Northern Hemisphere radiocarbon age calibration curve (0–55 cal kBP). *Radiocarbon*, 62(4), 725-757.
- Rollinson, H. R. (1993). *Using geochemical data: Evaluation, presentation, interpretation*. Singapore. Longman Scientific & Technical.
- Schillereff, D. N., Chiverrell, R. C., Macdonald, N., & Hooke, J. M. (2014). Flood stratigraphies in lake sediments: A review. *Earth-Science Reviews*, 135, 17–37. <https://doi.org/10.1016/j.earscirev.2014.03.011>
- Simonneau, A., Chapron, E., Vanni re, B., Wirth, S. B., Gilli, A., Di Giovanni, C., Anselmetti, F. S., Desmet, M., & Magny, M. (2013). Mass-movement and flood-induced deposits in Lake Ledro, southern Alps, Italy: Implications for Holocene palaeohydrology and natural hazards. *Climate of the Past*, 9, 825–840, <https://doi.org/10.5194/cp-9-825-2013>
- Sleeter, B. M., & Calzia, J. P. (2012). Klamath Mountains ecoregion. In B. M. Sleeter, T. S. Wilson, & W. Acevedo (Eds.), *Status and trends of land change in the western United States—1973 to 2000* (No. 1794-A-13, pp. 141–149). U.S. Geological Survey.
- St-Onge, G., Mulder, T., Piper, D. J. W., Hillaire-Marcel, C., & Stoner, J. S. (2004). Earthquake and flood-induced turbidites in the Saguenay Fjord (Qu bec): A Holocene paleoseismicity record. *Quaternary Science Reviews*, 23, 283–294. <https://doi.org/10.1016/j.quascirev.2003.03.001>
- Strasser, M., Monecke, K., Schnellmann, M., & Anselmetti, F. S. (2013). Lake sediments as natural seismographs: A compiled record of Late Quaternary earthquakes in Central Switzerland and its implication for Alpine deformation. *Sedimentology*, 60(1), 319–341. <https://doi.org/10.1111/sed.12003>
- Streig, A. R., Weldon, R. J., Biasi, G., Dawson, T. E., Gavin, D. G., & Guilderson, T. P. (2020). New Insights into Paleoseismic Age Models on the Northern San Andreas Fault: Charcoal Inbuilt Ages and Updated Earthquake Correlations. *Bulletin of the Seismological Society of America*, 110(3), 1077-1089.
- Struble, W. T., Roering, J. J., Black, B. A., Burns, W. J., Calhoun, N., & Wetherell, L. (2020). Dendrochronological dating of landslides in western Oregon: Searching for signals of the Cascadia AD 1700 earthquake. Geological Society of America
- Swain, D. L., Langenbrunner, B., Neelin, J. D., & Hall, A. (2018). Increasing precipitation volatility in twenty-first-century California. *Nature Climate Change*, 8(5), 427-433.
- Thomson, J., Croudace, I. W., & Rothwell, R. G. (2006). A geochemical application of the ITRAX scanner to a sediment core containing eastern Mediterranean sapropel units. *Geological Society, London, Special Publications*, 267(1), 65–77. <https://doi.org/10.1144/GSL.SP.2006.267.01.05>
- Toda, S. and Stein, R.S., 2013. The 2011 M= 9.0 Tohoku oki earthquake more than doubled the probability of large shocks beneath Tokyo. *Geophysical Research Letters*, 40(11), pp.2562-2566.

- Toonen, W. H., Winkels, T. G., Cohen, K. M., Prins, M. A., & Middelkoop, H. (2015). Lower Rhine historical flood magnitudes of the last 450 years reproduced from grain-size measurements of flood deposits using End Member Modelling. *Catena*, 130, 69–81.
- Topozada, T. R., Real, C. R., Bezore, S. P., & Parke, D. L. (1981). *Preparation of isoseismal maps and summaries of reported effects for pre-1900 California earthquakes* (Open-File Report No. 81-262). U.S. Geological Survey. <https://doi.org/10.3133/ofr81262>
- van Daele, M., Meyer, I., Moernaut, J., De Decker, S., Verschuren, D., & De Batist, M. (2017). A revised classification and terminology for stacked and amalgamated turbidites in environments dominated by (hemi) pelagic sedimentation. *Sedimentary Geology*, 357, 72–82. <https://doi.org/10.1016/j.sedgeo.2017.06.007>
- Vandekkerkhove, E., van Daele, M., Praet, N., Cnudde, V., Haeussler, P. J., & De Batist, M. (2020). Flood-triggered versus earthquake-triggered turbidites: A sedimentological study in clastic lake sediments (Eklutna Lake, Alaska). *Sedimentology*, 67(1), 364–389. <https://doi.org/10.1111/sed.12646>
- van der Weijden, C. H. (2002). Pitfalls of normalization of marine geochemical data using a common divisor. *Marine Geology*, 184(3–4), 167–187. [https://doi.org/10.1016/S0025-3227\(01\)00297-3](https://doi.org/10.1016/S0025-3227(01)00297-3)
- Wall, S. A., Roering, J. J., & Rengers, F. K. (2020). Runoff-initiated post-fire debris flow Western Cascades, Oregon. *Landslides*, 1–13.
- Wells, R. E., Blakely, R. J., Wech, A. G., McCrory, P. A., & Michael, A. (2017). Cascadia subduction tremor muted by crustal faults. *Geology*, 45(6), 515–518. <https://doi.org/10.1130/G38835.1>
- Wilhelm, B., Arnaud, F., Sabatier, P., Magand, O., Chapron, E., Courp, T., Tachikawa, K., Fanget, B., Malet, E., Pignol, C., Bard, E., & Delannoy, J. J. (2013). Palaeoflood activity and climate change over the last 1400 years recorded by lake sediments in the north-west European Alps. *Journal of Quaternary Science*, 28(2), 189–199. <https://doi.org/10.1002/jqs.2609>
- Wilhelm, B., Arnaud, F., Sabatier, P., Crouzet, C., Brisset, E., Chaumillon, E., ... & Delannoy, J. J. (2012). 1400 years of extreme precipitation patterns over the Mediterranean French Alps and possible forcing mechanisms. *Quaternary Research*, 78(1), 1–12.
- Wilhelm, B., Nomade, J., Crouzet, C., Litty, C., Sabatier, P., Belle, S., Rolland, Y., Revel, M., Courboulex, F., Arnaud, F. and Anselmetti, F.S., 2016. Quantified sensitivity of small lake sediments to record historic earthquakes: Implications for paleoseismology. *Journal of Geophysical Research: Earth Surface*, 121(1), pp.2-16.
- Wilhelm, B., Canovas, J. A. B., Aznar, J. P. C., Kämpf, L., Swierczynski, T., Stoffel, M., ... & Toonen, W. (2018). Recent advances in paleoflood hydrology: From new archives to data compilation and analysis. *Water Security*, 3, 1-8.
- Wirth, S. B., Girardclos, S., Rellstab, C., & Anselmetti, F. S. (2011). The sedimentary response to a pioneer geo-engineering project: Tracking the Kander River deviation in the sediments of Lake Thun (Switzerland). *Sedimentology*, 58(7), 1737–1761. <https://doi.org/10.1111/j.1365-3091.2011.01237.x>
- Wirth, S.B., 2013. The Holocene flood history of the Central Alps reconstructed from lacustrine sediments: Frequency, intensity and controlling climate factors (Doctoral dissertation, ETH Zurich).
- Wong, I. G. (2005). Low potential for large intraslab earthquakes in the central Cascadia subduction zone. *Bulletin of the Seismological Society of America*, 95(5), 1880–1902. <https://doi.org/10.1785/0120040132>
- Wright, H. E., Jr. (1967). A square-rod piston sampler for lake sediments. *Journal of Sedimentary Research*, 37(3), 975. <https://doi.org/10.1306/74D71807-2B21-11D7-8648000102C1865D>

Yeats, R. S. (2004). *Living with earthquakes in the Pacific northwest* (2nd ed.). Oregon State University Press.

Zolitschka, B. (1998). A 14,000 year sediment yield record from western Germany based on annually laminated lake sediments. *Geomorphology*, 22(1), 1–17. [https://doi.org/10.1016/S0169-555X\(97\)00051-2](https://doi.org/10.1016/S0169-555X(97)00051-2)

Tables

Table 1. Historic events with the potential to disturb the sediments of Lower Squaw Lake.

Event	Description	Date (CE)	
E1	Flood	#5 of 5 largest historic floods	2006
E2	Flood ^{1,2,4}	#2 of 5 largest historic floods	1997
E3	Local summer storm ²		1980s
E4	Flood ²		Late 1970s
E5	Flood	#4 of 5 largest historic floods	1974
E6	Lake drained to pre-dam level	All 17'	1972
E7	Flood ²	#1 of 5 largest historic floods	1965
E8	Flood	#3 of 5 largest historic floods	1955-6
E9	Flood; <i>debris dam failure</i>	#3 of 3; stream gage	1927
E10	San Andreas EQ	M7.9	1906
E11	Flood		1892
E12	Flood	#2 of 3; stream gage	1890
E13	Dam failure ³	Flood (winter rain-on-snow)	1881
E14	Dam installed ³	Raised the lake ~5 m	1877
E15	Brookings/Crescent City EQ	~M7.0 Intraplate EQ	1873
E16	Flood	ArKstorm; #1 of 3; stream gage	1861-2
E17	Cascadia EQ	~M9.0 subduction EQ	1700

¹An observer described water shooting out 10 feet past the dam, ²A local landowner described a thick layer of coarse sediment deposited over the entire Slickear Creek delta as looking like a “moonscape,” ³reported in the *Jacksonville Times* newspaper, and ⁴U.S. Forest Service personnel observed and removed logs that blocked the overflow at the dam, elevating the lake level by 3-4 feet. This flood caused the Applegate dam, located downstream from Lower Squaw Lake, to overflow and begin to erode the sediment on the sides of the dam (P. Jones; pers. communication, December 2019).

Table 2. Sediment core locations, water depths, and lengths.

Core name	Type	Length (m)	Water depth (m)	Latitude (°)	Longitude (°)
SQB-ss	Surface core	0.80	16.9	42.04405	-123.01853
SQB1	Livingstone	6.74	16.9	42.04405	-123.01853
SQB2	Livingstone	7.37	16.5	42.04405	-123.01853
SQB5	Livingstone	3.98	23.5	42.04264	-123.01909
SQB6	Livingstone	5.51	10.5	42.04336	-123.01732
SQB8	Kullenberg/Gravity	8.01	30.0	42.04227	-123.01908
SQB9	Kullenberg/Gravity	8.29	37.0	42.03982	-123.02050
SQB10	Kullenberg/Gravity	10.08	35.0	42.03857	-123.02108
SQB11	Kullenberg/Gravity	7.55	29.2	42.03778	-123.02175
SQB12	Kullenberg/Gravity	5.24	~20.0	42.04191	-123.01864
SQB13	Kullenberg/Gravity	6.24	25.0	42.02056	-123.02056
SQB14	Kullenberg/Gravity	8.28	30.0	42.04356	-123.01836
SQB15	Kullenberg/Gravity	4.55	28.5	42.04197	-123.01945

Cores highlighted in bold text are those identified by orange circles in Figure 5. *Cores SQB4 and SQB7 are not included in this list because they are less complete due to partial recovery compared to cores SQB5 and SQB6 (from the same locations). Note: SQB-ss is a surface sample (push core). Kullenberg cores are mildly to moderately disturbed at the top because the coring tubes collapsed some during coring. Sediments in the deeper water cores contained methane; when cutting coring tubes into sections, some sediment was extruded and captured in small subsections.

Table 3. Background sediment characteristics.

		Wet density <i>g/cm³</i>	Dry density <i>g/cm³</i>	%Water	% Organic	% CaCO ₃	% Inorganic	Mag susc (<i>S</i>)	CT (<i>HU</i>)
After inflection	Ave	1.13	0.34	70.01	14.48	10.74	74.78	-2×10^{-5}	~400
(<i>n</i> = 13)	<i>SD</i>	0.02	0.04	3.34	1.29	1.96	1.89		
Before inflection	Ave	1.05	0.22	79.42	22.33	17.20	60.47	-10×10^{-5}	~200
(<i>n</i> = 9)	<i>SD</i>	0.02	0.03	0.83	3.23	2.55	3.80		

Mag susc = magnetic susceptibility; CT = computed tomography density. Diatom tests were not removed from samples prior to combustion; therefore inorganic:organic data include a small influence from the remaining silica from diatoms in the percentage-inorganic data (estimated to be less than 6%). CT density is expressed in Hounsfield Units (HU). Note: Organic, inorganic and CaCO₃ percentages were calculated from dry weights. Percent inorganic data does not include percent CaCO₃.

Table 4. Age control data. The sample in gray text (Sample 0) was not included in the age model because it is much older than the others in the sequence. Samples 1–4 were used to create the age-depth model, and the other ages were used to align the sections shown in Figure 6.

Sample #, section ID and depth in section	Depth, cm (composite)	Depth, cm (event free)	Description	Laboratory and sample no.	¹⁴ C yrs BP
0 SQB1A; 14.0-14.5 cm	85-85.5	64	Fir needle	S-ANU 42418	865+/-35
1 SQB1A; 15.5-16.0 cm	86-86.5	65	Fir cone frag	S-ANU 42419	255+/-25
2 SQB1A; 25.5-26.0 cm	96.5-97	71	Fir needle	S-ANU 42618	110+/-25
3 SQB1A; 35.5-36.0 cm	106.5-107	81	Fir needle	S-ANU 42617	190+/-25
4 SQB1A; 84.0-85.0 cm	155-156	101	Fir needle	S-ANU 42616	260+/-40
5 SQB1A; 95.0-96.0 cm	166-167	115	decid. plant frags	S-ANU 42417	630+/-25
6 SQB1B; 67.0-68.0 cm	254-255	185	plant frags	UCIAMS 140214	1155+/-20
7 SQB5C; 27-28 cm	263-264	194	Cone bract	NOSAMS	1270+/-20

Table 5. Splice data for SQB1/2/ss composite as shown in Figure 6. Section SQB1-A is the only section in this core that was used to create the composite core. SQB2A 101 cm is at the same stratigraphic location as SQB1-A 56 cm, as shown in Figure 6 (which is a graphical representation of the relationships between sections presented in the SQB1/2/ss splice represented by this table). Note that SQB-ss is expanded relative to cores SQB1 and 2 and was compressed to match stratigraphy as shown in Figure 12a.

¹ Composite depth (cm)	² Composite depth (cm)	Core section	Depth in section (cm)	Core section	Depth in section (cm)
0	0			SQB-ss	0
33	26	SQB2-A	2	SQBss	33
103	97	SQB2-A	72	SQB1-A	24
135	129	SQB2-B	4	SQB1-A	56

¹Composite depth (cm) without adjusting the length of section SQB-ss; ²Composite depth (cm) after compressing section SQB2-ss to match the stratigraphy of SQB2-A.

Table 6. XRD mineralogy.

	Classification	Formula
Lake bedrock:		
Clinochlore – 1Mllb, ferroan	Chlorite grp	$Mg_5Al(AlSi_3O_{10})(OH)_8$
Quartz, syn	Silicate	SiO_2
Chlorite-serpentine	(greenschist)	$(Mg,Fe)_3(Si,Al)_4O_{10}(OH)_2 \cdot (Mg,Fe)_3(OH)_6$
Muscovite-2M1, 3T	phyllosilicate	$KAl_2(AlSi_3O_{10})(F,OH)_2, (KF)_2(Al_2O_3)_3(SiO_2)_6(H_2O)$
Watershed bedrock:		
Clinochlore – 1Mllb, ferroan	Chlorite group	$Mg_5Al(AlSi_3O_{10})(OH)_8$
Quartz, syn	Silicate	SiO_2
Ferro-actinolite	Fe-rich amphibole	$Ca_2(Mg_{2.5-0.0}Fe_{2+2.5-5.0})Si_8O_{22}(OH)_2$
Albite, calcian, ordered	Plagioclase feldspar	$NaAlSi_3O_8$
Pottassicpargasite	Ca amphibole	$KCa_2(Mg_4Al)(Si_6Al_2)O_{22}(OH)_2$

XRD mineralogy for single samples of lake and watershed bedrock, and samples of sediment taken from Core SQB2 (light gray, dark gray and basal gravel units). The lake bedrock is a quartz muscovite schist with chlorite minerals, and the watershed bedrock is composed of chlorite minerals, plagioclase, and Fe- and Ca-amphiboles.

Table 7. Unmodeled and modeled calendar age distributions for radiocarbon (RC) samples 1-4. Agreement (Amodel) indices represent the % overlap between the modeled and unmodeled distributions.

a. OxCal P_sequence results.

RC #	Unmodeled (AD)	Modeled (AD)	Amodel
RC sample 1	1523 -	1770 - 1800	54
RC sample 2	1682 - 1935	1680 - 1780	52.9
RC sample 3	1654 -	1650 - 1770	88.1
RC sample 4	1492 -	1490-1670	113.1

b. OxCal P_sequence results with 1700 CE used as a calendar date (C_date) in the model in place of radiocarbon sample 2.

RC #	Unmodeled (AD)	Modeled (AD)	Amodel
RC sample 1	1523 – 1800	1770 – 1800	60
RC sample 2	C_date = 1700 CE		
RC sample 3	1652 -	1660 – 1690	101.8
RC sample 4	1495 -	1520 – 1670	101.9

Amodel is the model agreement index used to see if the model as a whole is not likely given the data, and should usually be over 60%.

Table 8. Event ages for deposits A-J based on the age model shown in Figure 16.

Event ID	Mean	Median	Min	Max
A			1980	2013
Between A/B	1970	1970	1954	1985
B				
C	1920	1920	1870	1970
D	1900	1900	1860	1960
E	N/A			
F	1870	1870	1830	1930
G	1920	1860	1830	1910
H	1850	1850	1820	1890
I	1850	1850	1820	1890
J	1740	1720 (1780)*	1680	1780

*Multiple peaks

Table 9. Table of deposit characteristics and attributions.

	Attribution	Grading	Basal contact	XRD	Color ²	CT density (HU)	Magnetic susc. ³ scaled to CT density	Particle size and sorting
A	1997 CE Flood	normal	Sharp; erosive	Mixed	Brown; darker in the lower half (organics)	High (~8-900) throughout	High throughout, but rises slowly from the base upward (compared to density)	Dominated by coarse silt, capped by a thin layer of fine-grained silty clay. Thin layer of coarse silt and fine sand at base.
B	1964 CE Flood	normal	Sharp; erosive	Mixed	Brown; darker in the lower half (organics)	High (~8-900) throughout	High throughout, but rises slowly from the base upward (compared to density)	Dominated by coarse silt, capped by a thin layer of fine-grained silty clay.
C	1927 CE Flood	normal?	Wavy; discontinuous	N/A	Slightly grayer than background	Moderately high	Similar to density, but lower amplitude	Too thin to sample for accurate particle size; missing in core SQB5 (eroded from section).
D	1906 CE San Andreas EQ	normal?	Wavy; irregular	Watershed	Orange	Moderately high	Slight increase	Three discontinuous wavy layers: the lower layer is orange in color and composed of fine-medium grained silt.
E	Local wall failure deposit?	normal	Sharp; erosive	Schist	Dark Gray	Moderately high	Slight increase	Visible mica flakes in this unit. This unit is observed in only one core (SQB5), which is near a steep slope. CT density increases but magnetic susceptibility change is subtle.

	Attribution	Grading	Basal contact	XRD	Color ²	CT density (HU)	Magnetic susc. ³ scaled to CT density	Particle size and sorting
F	uncertain	normal	Sharp	N/A	Medium Gray	High	Slight increase	Thin and difficult to characterize; different thickness in each core. CT density increases, but magnetic susceptibility change is subtle. Load structures at base.
G	1881 flood and dam failure	reverse, then normal	Indistinct	N/A	Faint	Moderately high; rounded profile	Indistinct, but similar to density	Particle size data N/A. Slightly stiffer higher density sediment; peak density midunit.
H	1873 CE intraplate earthquake	normal	Sharp	Watershed	Light Gray	High	Similar to density, but lower amplitude	Medium silt; fines entrained above basal silt.
I	1873 CE intraplate earthquake	reverse, then normal	Sharp; erosive	Schist	Dark Gray	High	Similar to density, but lower amplitude	Coarse silt, poorly sorted. In some cores reverse, then normal grading.
J	1700 CE Cascadia Earthquake	normal	Sharp	Watershed	Light Gray	High (~8–900)	High; correlated with CT density	Basal silt is very fine-grained and well-sorted, becoming less-well sorted upward. Load structures at base.

¹See Figure 12. ²Brown = 2.5Y 3/2, Light Gray = 2.5Y 4/1, Dark Gray = Gley 2 4/5PB, Orange = 5Y 4/1. Variations in colors through deposits were visibly obvious but frequently difficult to differentiate from one another using Munsell color charts.

³Magnetic susceptibility variability was compared to the variability in CT density. Note that magnetic susceptibility data is influenced by surrounding sediment (exponential decrease with distance), and therefore the magnitude can be influenced by the thickness of the unit if thin (~1 cm or less; see Figure 13). The most diagnostic features of the earthquake-triggered deposits is that they were determined to have a watershed composition (by XRF).

Figures

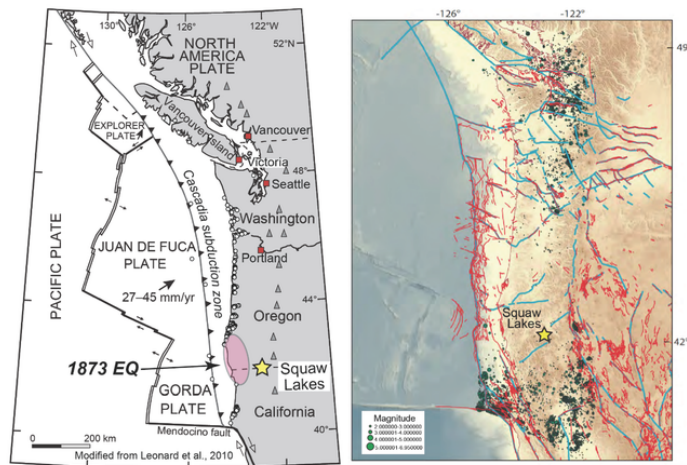


Figure 1.

Figure 1

Location Map. Left: Map showing the location of Squaw Lakes with respect to the Cascadia subduction zone. Upper and Lower Squaw Lake are located in southern Cascadia approximately 180 km inland east of the deformation front. The open circles indicate the locations of coastal paleoseismic sites (base map modified from McCrory et al., 2014). The pink oval represents the approximate location of the hypocenter for the 1873 “Brookings” intraplate earthquake. Right: Faults from a simplified Cascadia forearc fault model (blue) on upper-plate forearc seismicity (1975–2009). Squaw Lakes are located at about 35 km above the transition from the seismically to aseismically slipping reaches of the plate interface. Figure adapted from Data Repository Figure 3c by Wells et al., 2017; Mb > 2.0 from McCrory et al. (2012). ; USGS Quaternary Fault database (red lines).

Figure 2

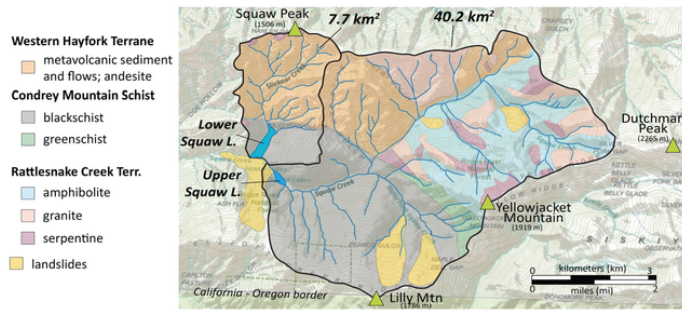


Figure 2

Geologic and Geomorphic Setting. Upper and Lower Squaw Lakes are situated in the Condrey Mountain Schist, however the bedrock of the lake catchments consists of distinctive metamorphic and plutonic lithologies. Note the large landslide responsible for lake creation. Geology from Donato, 1993.

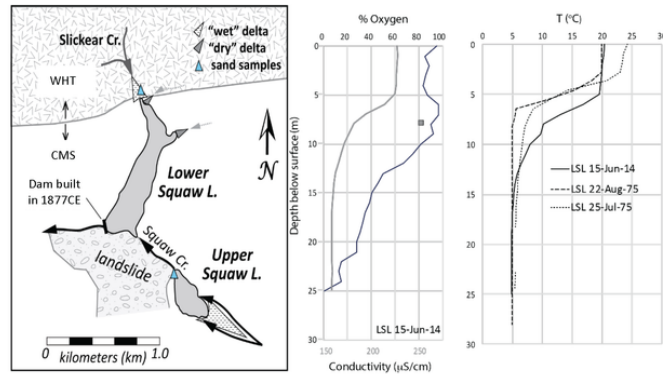


Figure 3.

Figure 3

Left. *Upper Squaw Lake and Lower Squaw Lake can be thought of as a single system, with the landslide between them functioning as a sill separating the two basins.* Upper Squaw Lake is fed by Squaw Creek, which forms a large sandy delta ~0.5 km long as it enters the lake from the southeast. Squaw Creek continuously flows between the two lakes, transporting water and sediment from Upper Squaw Lake to the southern end of Lower Squaw Lake. Blue triangles indicate the locations of sand samples taken to determine sediment provenance. CMS: Condrey Mountain Schist, and WHT: Western Hayfork Terrane. Wet deltas are saturated and dry deltas are not (inferred from vegetation types). **Right.** Temperature, conductivity and % oxygen for Lower Squaw Lake. Data collected in 2014 were supplemented by data from Larson (1975). The lake is stratified with a thermocline between 5-7m water depth. At this same depth an unstable spike in conductivity was measured (left) indicating the presence of groundwater flowing into the lake at that depth.

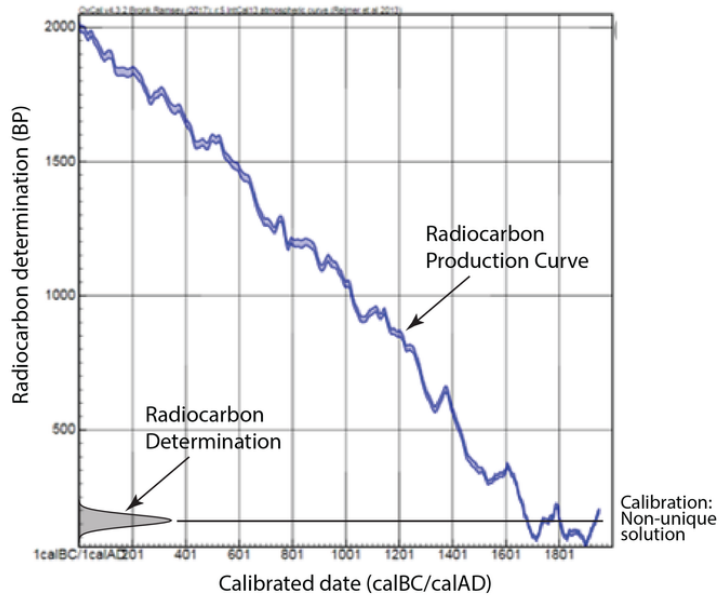


Figure 4.

Figure 4

Non-unique calibration results from variability in the radiocarbon production curve (IntCal13 shown; Reimer et al., 2013).

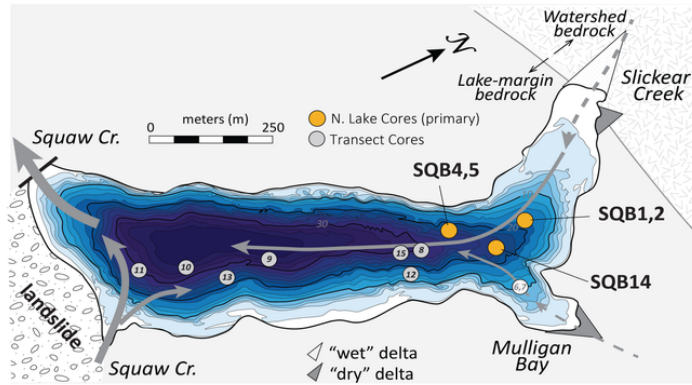


Figure 5.

Figure 5

Core locations. Cores were collected along a north–south transect. The primary core sites are identified by the orange circles, and the other cores collected are identified by the numbered gray circles.

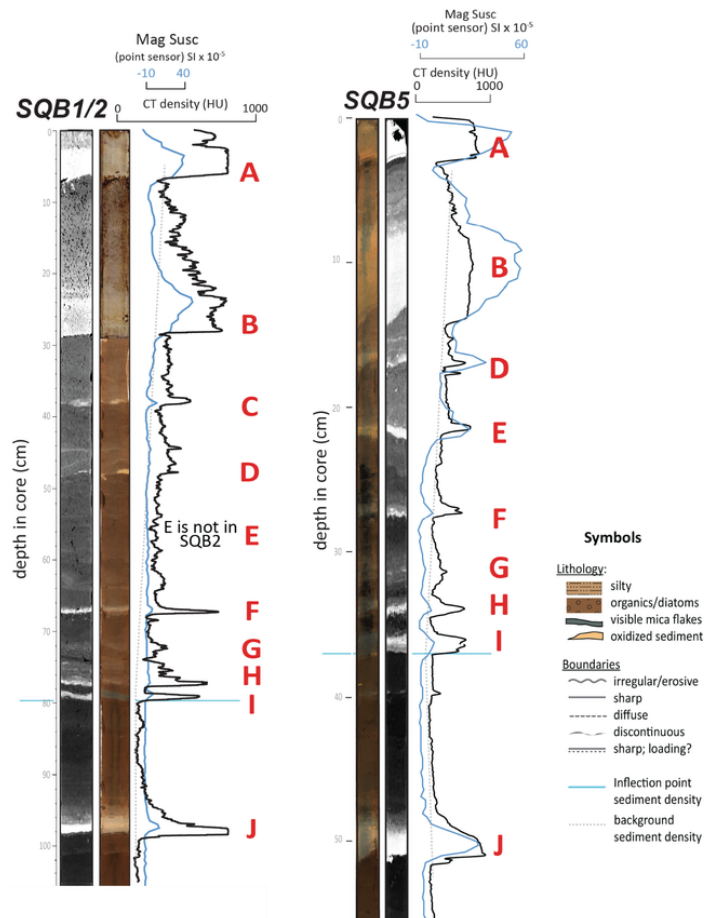


Figure 6.

Figure 6

Disturbance deposits A-J were identified as excursions in CT density and magnetic susceptibility in cores SQB1/2 and SQB5. Note that deposit C, present in core SQB2, is missing from core SQB5, and deposit E is missing from core SQB1/2. The dashed line reflects background sediment density and an inflection can be seen in the trend near deposits H and I.

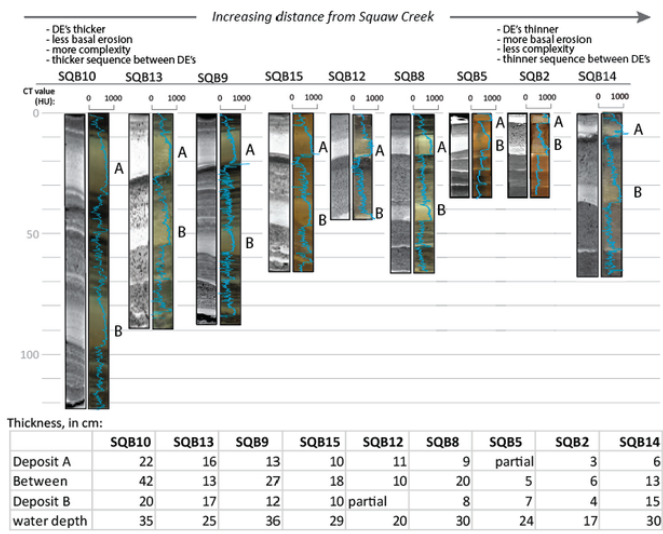


Figure 7.

Figure 7

Two distinctive lake-wide inorganic disturbance event deposits (DE's) are found in the upper portions of all cores. Event deposits and interevent sediment thicknesses are all greater to the south and in the deeper water cores.

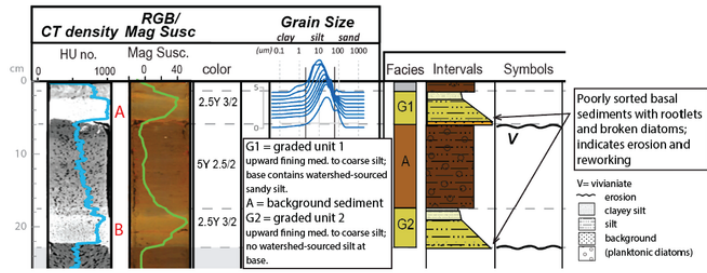


Figure 8.

Figure 8

Deposit types A and B in the surface core SQBss (at the location of cores SQB1 and SQB2). Facies types G1 and G2 are very similar, other than the presence of a thin layer of sandy silt at the base of deposit A.

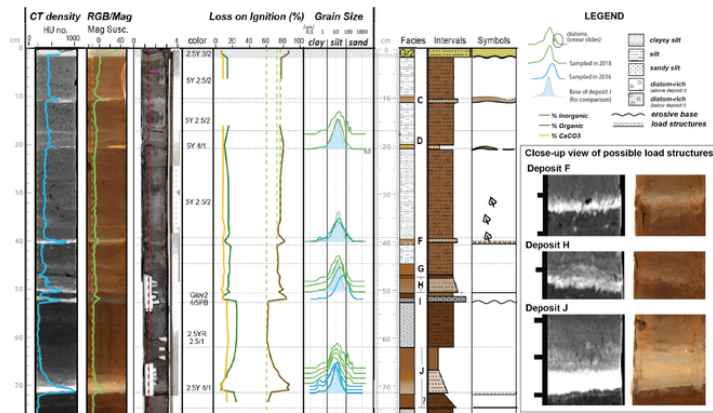


Figure 9.

Figure 9

Deposits C-J in SQB2. Core log data for section SQB2A showing the locations and types of data that exist for this section. Particle-size data are shown as distributions rather than ratios or median sizes to show how they compare to the size and narrow range shown for deposit J (shown as a light blue shaded distribution). The interval widths at the right show a combination of density and grading characteristics: wider intervals are denser and coarser grained; narrower intervals are finer grained with lower density.

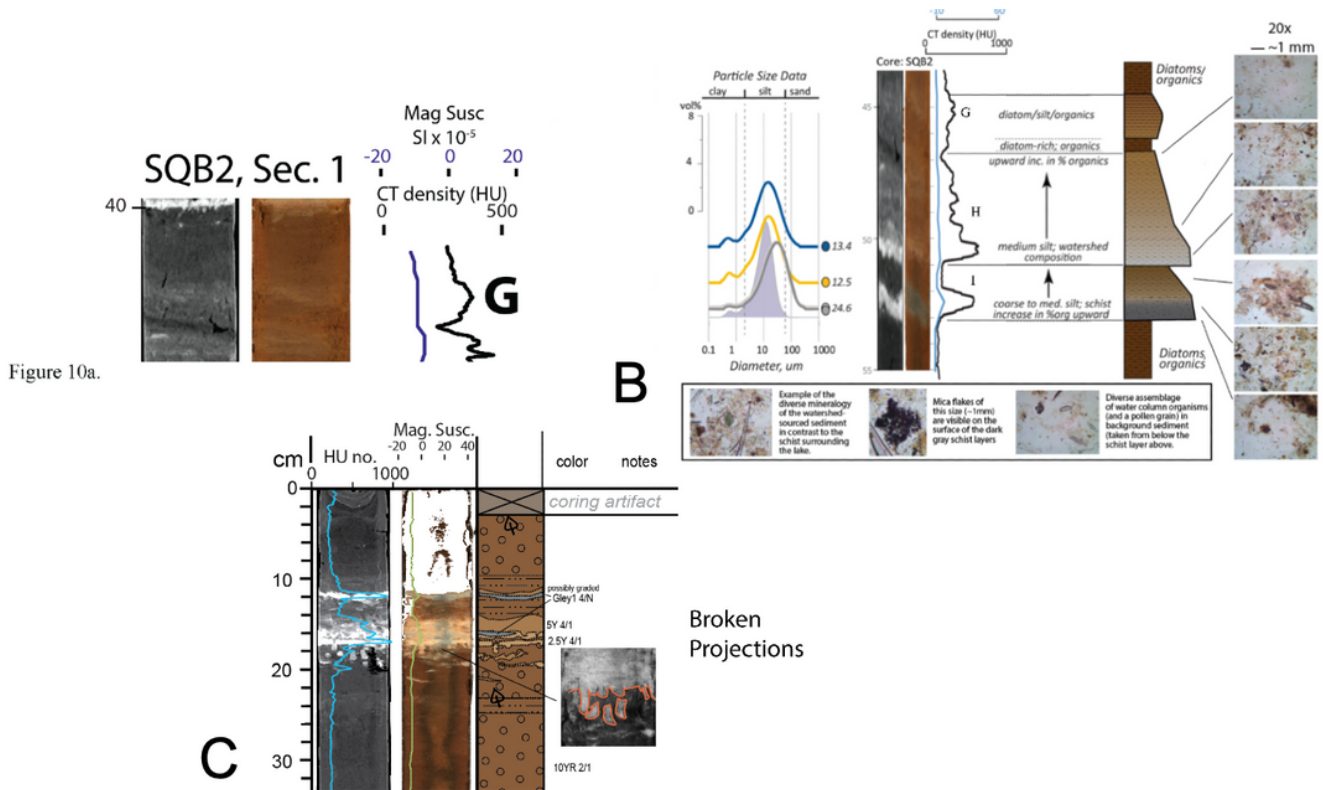


Figure 10

10a. Deposit G in core SQB2, section 1.

10b (previous page). Deposits G, H and I in core SQB2. This figure shows particle-size distributions from the layers shown in core SQB2 (median particle size, in mm, is shown to the right of the colored dots). The blue (filled) distribution represents the particle-size distribution for disturbance J (shown for comparison). To the right of the core imagery and sediment descriptions is a schematic representation of the core where excursions to the right represent denser sediment. The smear slides show that the composition of the disturbance deposits varies in mineralogy and organic content. Note the different species of diatoms in the smear slide taken from the very top of the sequence (between disturbances G and H). The lower panel zooms into details of the smear slides shown at the far right of the schematic. Note that the width of the schematic diagram of the core (to the left of the smear slides) represents sediment density.

10c. Other evidence of an earthquake influence in the sedimentary record. a) Folded sequence, b) a 1 cm thick layer of organic matter and benthic diatoms suggests the reworking of shallow water sediment in addition to the fine silt of the deposit suspected to be the result of liquefaction (the light colored silt), c) broken projections in the organic sediment below – load structures.

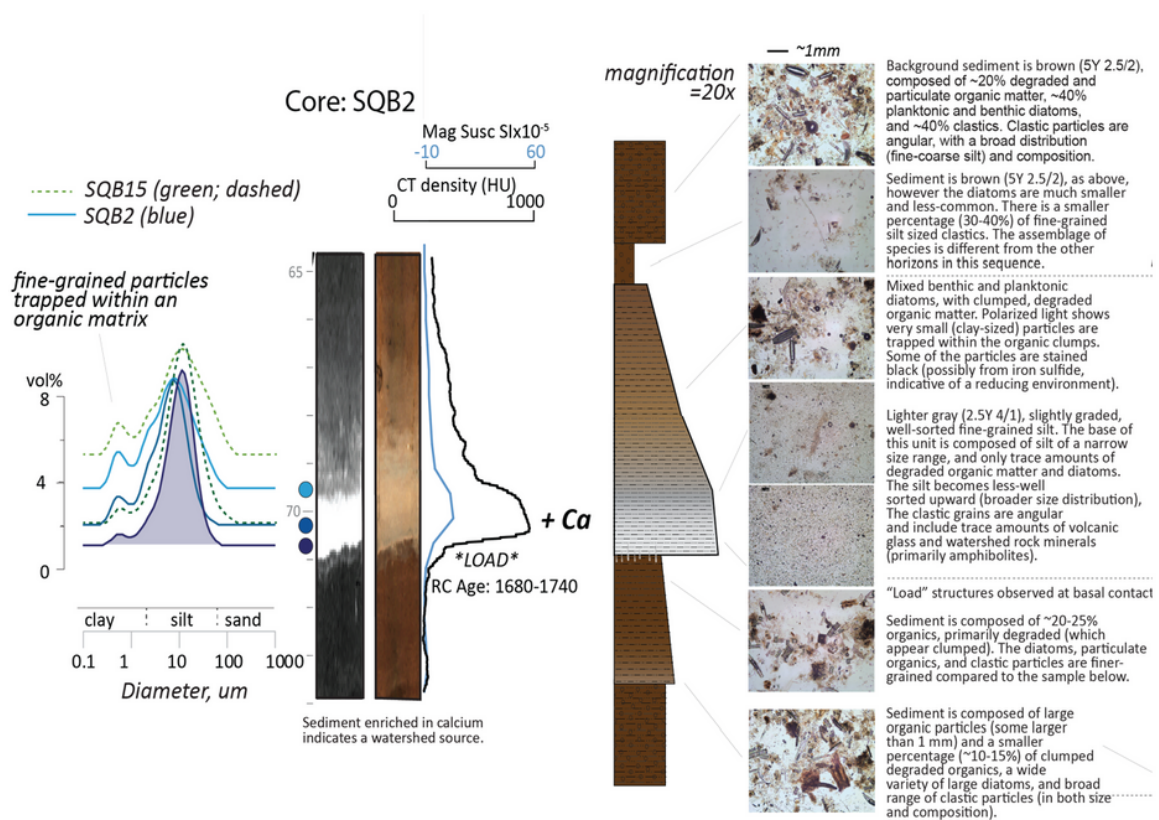
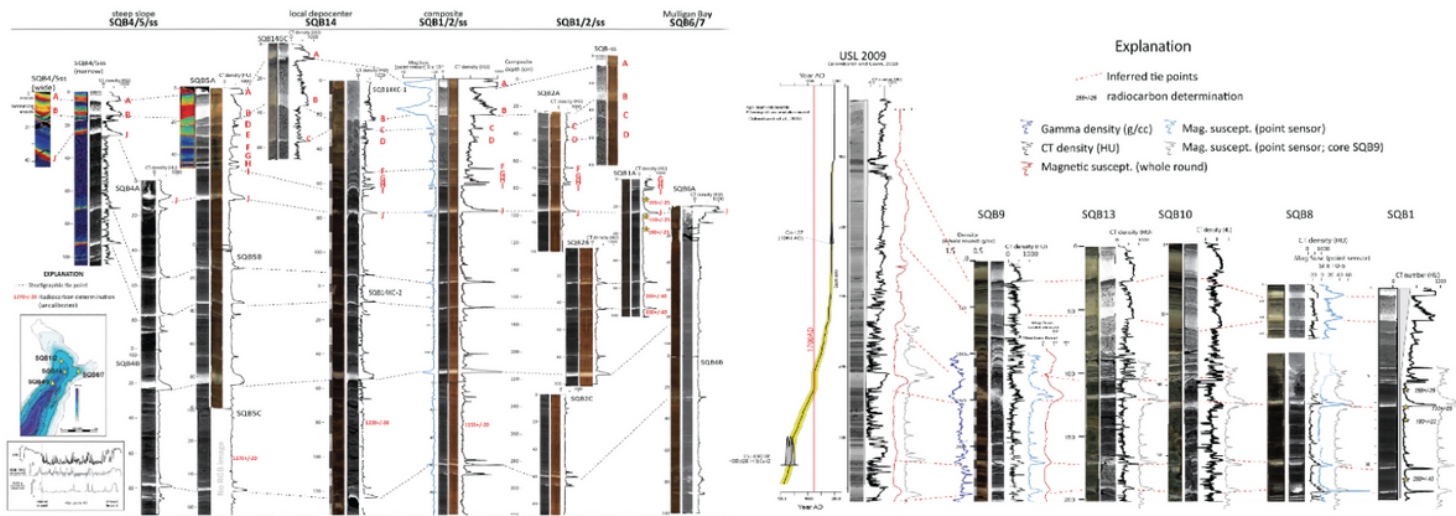


Figure 11

(previous page). Particle-size data, core imagery, physical properties, and schematic with smear slides and detailed descriptions of sediment composition for deposit J. Note that the sediment bleeds into the organic sediment below, suggesting loading of the dense silt into the organic matter. Note that the silt is fine grained and pure at the base compared to the more sediment above. The width of the schematic diagram of the core (to the left of the smear slides) represents sediment density.



A

Figure 12b.

Figure 12

12a (previous page). Tie points between northern core sections, SQB9 and the composite core created from SQB1, SQB2, and the surface sample. Each section in the northern cores is represented in this figure by a grayscale image of sediment CT density (brighter = higher density, darker = lower density), CT density traces (black lines; higher density to the right) through the core [in Hounsfield Units (HU)], and RGB color image. Note the strong similarity between each ~1-m section.

12b. Lake-wide tie points. This figure shows the age-depth model, CT imagery and physical property data for the Upper Squaw Lake (USL 2009) core compared to key cores in Lower Squaw Lake. All lines are dashed to indicate uncertainty, however the relationships between the lower lake cores are more certain than the relationship to the upper lake core because each of the cores has two distinct upper units that correlate to one another. Note that each of the cores has the same pattern of disturbances as indicated by the ghost trace from SQB9.

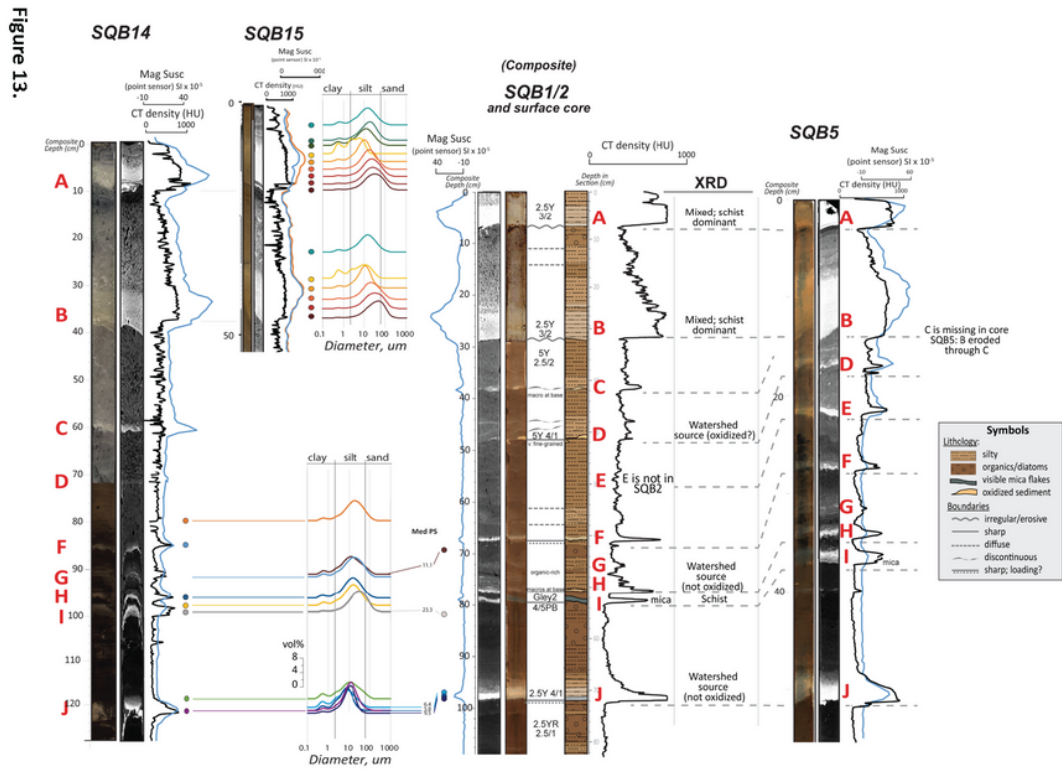


Figure 13

Sedimentological data for the northern cores. CT density was acquired from sediment cores while still as whole-round sections, and therefore contains methane pockets. These pockets are very low density compared to the sediment and are the source of CT density noise in Core SQB14 (especially between 40 and 85 cm in this figure).

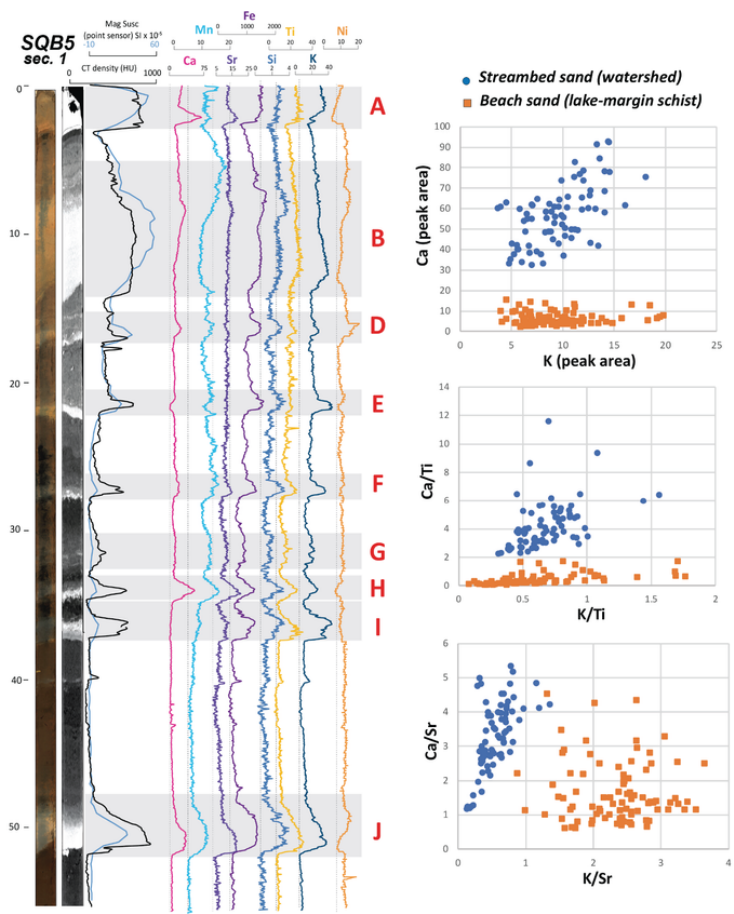


Figure 14.

Figure 14

X-Ray Fluorescence data for core SQB5, Sec. 1. **Left:** Photograph, CT image, density (black trace) magnetic susceptibility (blue line), and raw XRF data (peak area) for eight elements are shown in colored lines. **Right:** Calcium and potassium from watershed and beach sand samples do not overlap, whether data are represented as raw counts (peak area) or normalized by titanium or strontium.

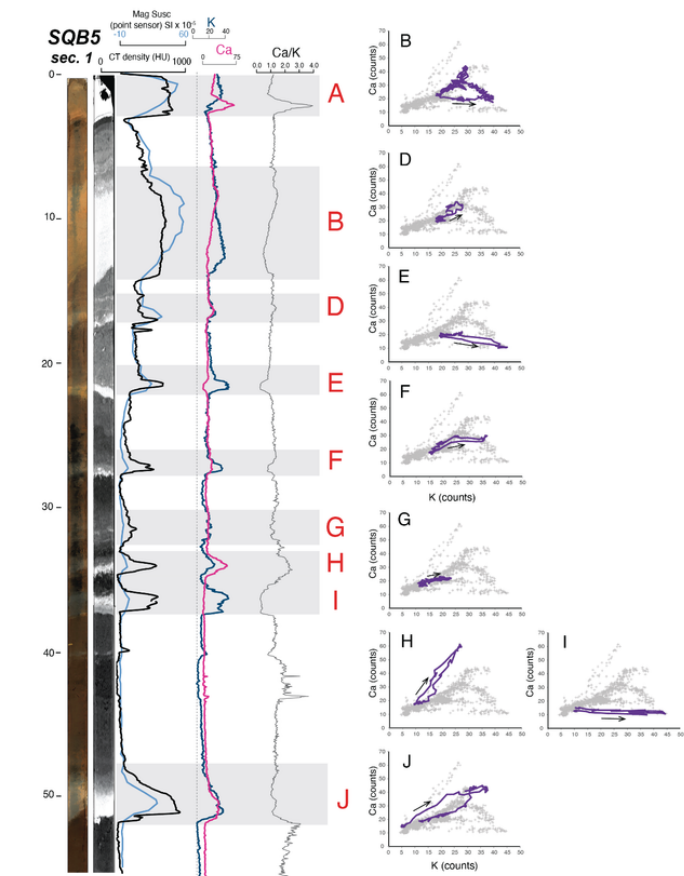


Figure 15.

Figure 15

XRF scatterplots for deposits B-J in core SQB5. Each of the gray bars represents the base and top of the event deposits B-J based on where the disturbance deposit starts and ends with respect to the scatterplots (raw, unsmoothed data) at right. Also shown are end member variables Ca and K and their ratio, Ca/K to express the relationship between them. Note that the scatterplot data are not smoothed to show the true variability in the data. Scatterplots and their interpretations are described in more detail in the Discussion section.

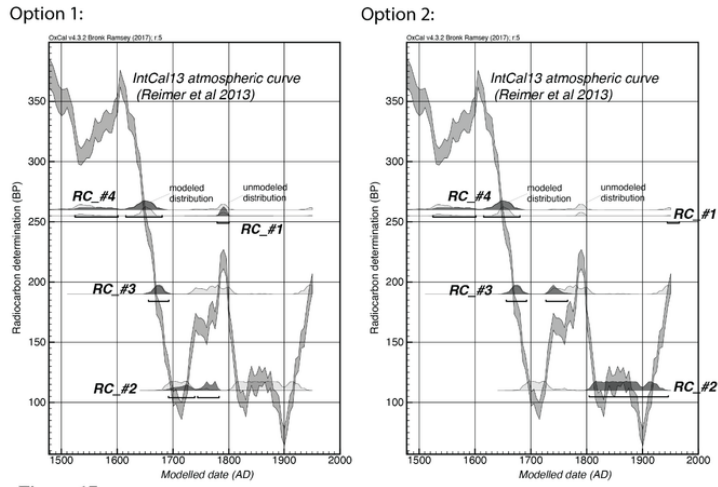


Figure 17.

Figure 17

Options for radiocarbon calibration assuming samples died close to the time surrounding sediment was deposited. Option 1 is the result of the OxCal P_sequence age-depth model presented in Figure 16, and Option 2 is the alternative. Because the event-free sediment thickness is 71 cm (representing hundreds of years, Option 1 is considered most likely. See text.

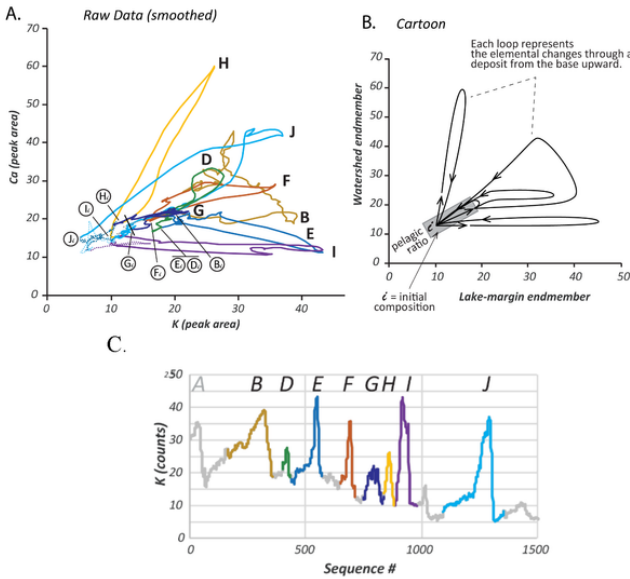


Figure 18.

Figure 18

XRF scatterplots. Colored lines represent the individual disturbance deposits. A) Variability through the disturbance deposits in core SQB5 can be expressed in terms of the endmembers K and Ca (shown after smoothing). Each of the deposits shows variability that is unique and related to the initial composition of the disturbed sediment, sediment partitioning, or additional inputs during deposition. B) This cartoon show how patterns in the data may be interpreted from the base of an event to the top. Arrows show the direction with depth from the base of the deposit to the top (see Figure 15) Each deposit begins at the initial background ratio between Ca and K, and increases and decreases along a distinctive path, before the deposit ends where composition returns to the initial background ratio. A suggested explanation for these patterns is that they reflect the relative amounts of each variable, and a third implicit variable related to sediment density. C) Key to colors represented by the data shown in A); the vertical axis is K (raw counts), and the horizontal axis is the step number in the sequence downcore.

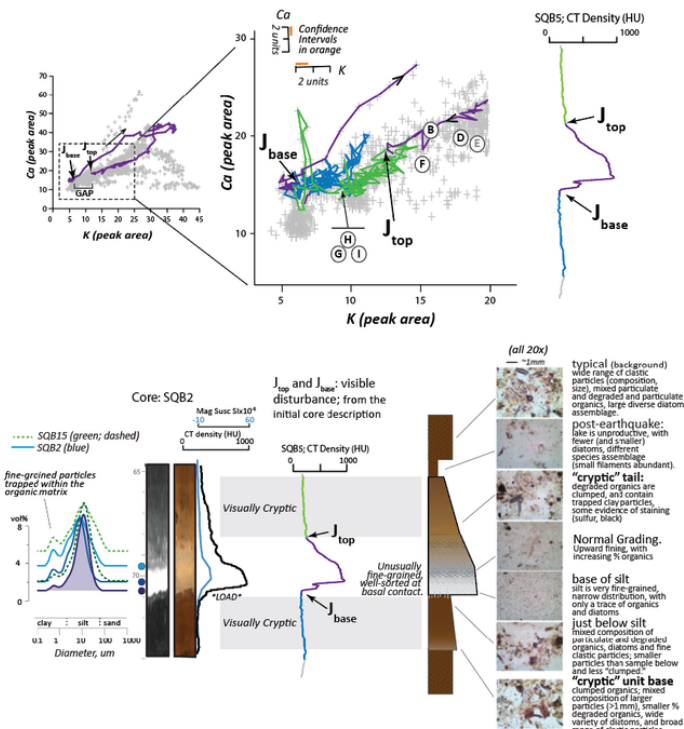


Figure 20.

Figure 20

Deposit J is a complex sequence. A gap exists between the initial and final ratios, which can be filled in by including the sediment below (identified in blue) and by interpreting the upper unit to have a long tail (shown in green). The base of the clastic unit is very well-sorted and fine-grained and appears to “bleed down” from the clastic base into the very fine, organic-rich sediment below suggesting it is the result of loading. The tail of the deposit is followed by a change in the size and types of diatoms and other components suggesting a post-earthquake change in water column organisms. Much of this complexity was not apparent from smear slide or sedimentological observations of the core material. Note that the data in the scatterplot are not smoothed to show the true variability of the data.

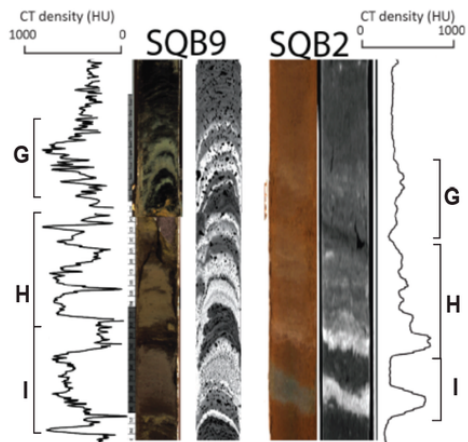


Figure 21.

Figure 21

Deposits G, H and I. A comparison to deeper water core SQB9 (selected because it is at the lake depocenter and less likely to be missing sediment due to erosion) suggests that deposits H and I are the result of a landslide dam failure and either reflection deposits (from a seiche), post-dam-failure turbidites arriving from several locations in the lake, or retrogressive landslides after the toe of the landslide became destabilized after the landslide dam failed.

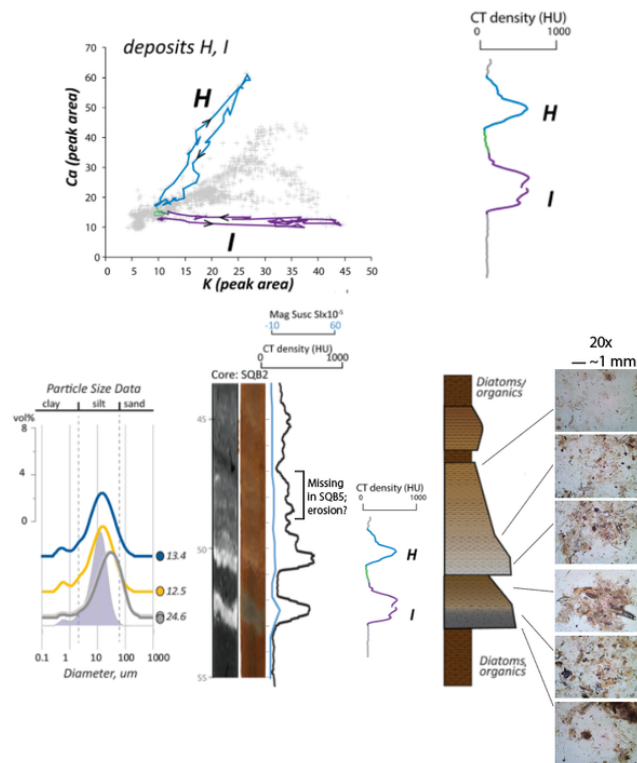


Figure 22.

Figure 22

Characteristics for disturbance event deposits H and I. These deposits appear to be triggered closely spaced in time because sediment composition does not stay at background levels, but instead transitions immediately into deposit H. The low-density layer between H and I is an organic-rich layer containing a high percentage of organics, with a thin layer of plant macrofossils just before the watershed-sourced medium-grained silt is deposited. This suggests there was enough time for leaves to settle prior to the deposition of deposit H. Top: XRF loop for H (blue) is clockwise, while the loop for I is counterclockwise, suggesting a different depositional mechanism. The purple shaded particle size data is from deposit J for comparison to the grainsize data from deposits H and I. Note that the horizontal axis for the cartoon of the deposit sequence (bottom right) represents sediment density.

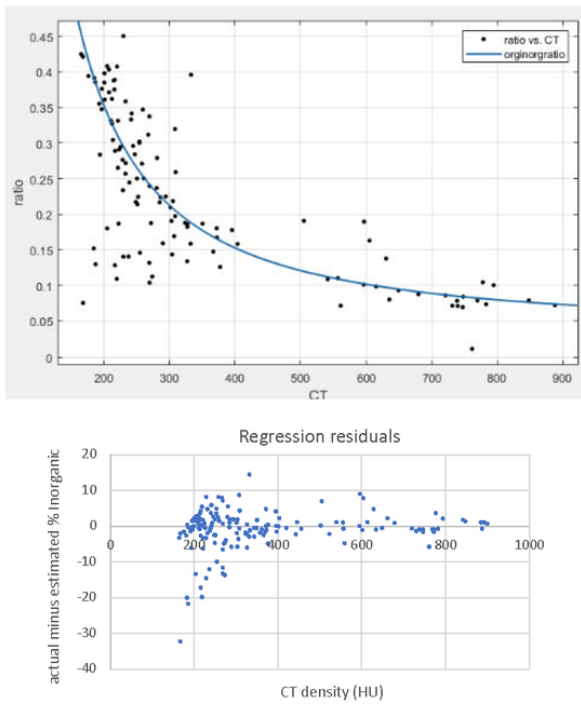


Figure 23.

Figure 23

A regression equation was used to estimate the % inorganic content from CT density data (top). This equation explains 97% of the variance. Some points are not well-described by this relationship, which can be seen in the residuals (bottom) as well as inorganic content (ratio of inorganic to organic sediment) versus CT density. This may be because of challenges of getting CT density and inorganic content data aligned or could be because % calcium carbonate was not included in the regression.

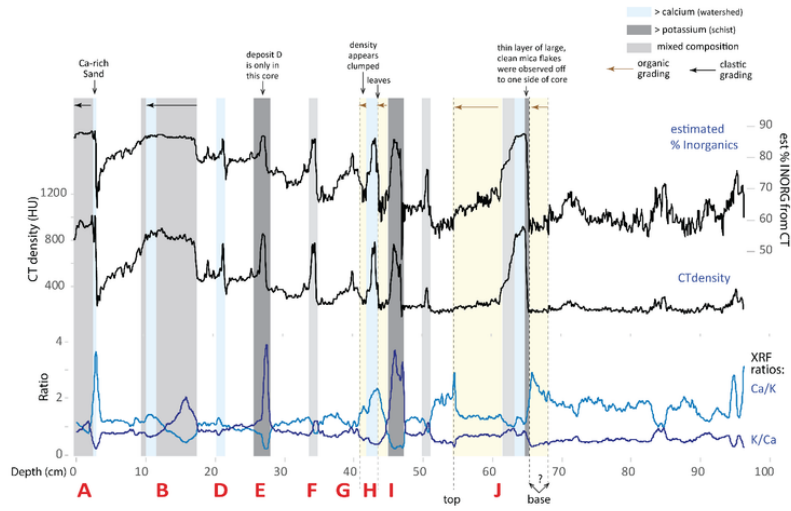


Figure 24.

Figure 24

Deposit boundaries and organic grading. I used CT density (middle) to estimate the inorganic content in core SQB5 (top). Dark gray bars identify deposits enriched in potassium and blue bars identify deposits enriched in calcium. Yellow identifies those deposits that have organic grading. Deposit D is too small to determine if it has organic grading.

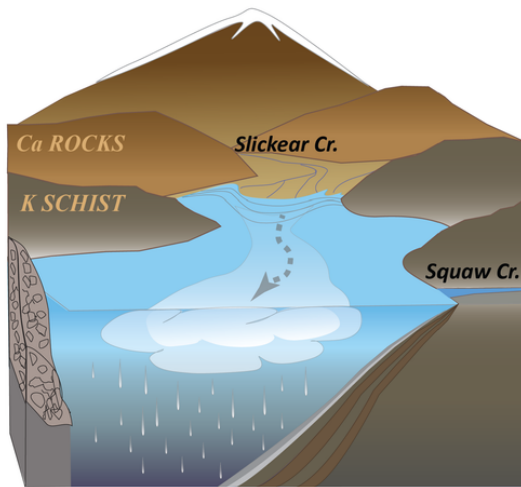


Figure 25.

Figure 25

Inferred mechanisms controlling deposit J. 1) Initial shaking causes a small turbidite, which is 2) followed by the release of watershed-sourced sediment and groundwater from the lake's large delta at the thermocline. 3) Energy in the water column, possibly an internal wave, causes sediment to be partitioned in the water column as it settles. 3) Waning ground motions allow settling of the organic rich tail, then finally 4) the water column returns to pre-earthquake conditions.

Supplementary Files

This is a list of supplementary files associated with this preprint. Click to download.

- [Moreysupplementarydata.docx](#)